ORIGINAL ARTICLE

Allanite U–Pb dating places new constraints on the high-pressure to high-temperature evolution of the deep Himalayan crust

Eleni Wood[1] | Clare J. Warren[1] | Barbara E. Kunz[1] | Tom W. Argles[1] | Anna Bidgood[2,3] | Alison Halton[1] | Samantha J. Hammond[1] | Ian L. Millar[4] | Nick M. W. Roberts[4]

[1]School of Earth, Environment and Ecosystem Sciences, The Open University, Milton Keynes, UK

[2]Carnegie Institution for Science, Washington, District of Columbia, USA

[3]Irish Centre for Research in Applied Geoscience, University College Dublin, Dublin, Ireland

[4]Geochronology and Tracers Facility, British Geological Survey, Keyworth, Nottingham, UK

Correspondence
Clare J. Warren, School of Earth, Environment and Ecosystem Sciences, The Open University, Milton Keynes MK7 6AA, UK
Email: clare.warren@open.ac.uk

Abstract

During continental collision, crustal rocks are buried, deformed, transformed and exhumed. The rates, timescales and tectonic implications of these processes are constrained through the sequence and conditions of metamorphic reactions in major and accessory phases. Petrographic, isotopic and elemental data from metabasite samples in NW Bhutan, eastern Himalaya, suggest initial equilibration under high-pressure (plagioclase-absent and rutile-present) conditions, followed by decompression to lower pressure conditions at high-temperatures that stabilized plagioclase, orthopyroxene and ilmenite. Field observations and chemical indicators suggest equilibration under the lower pressure conditions is likely linked to the infiltration of melt from the host metasedimentary rocks. The metabasites preserve two metamorphic growth stages of chemically-and petrographically distinct allanite that temporally overlap two stages of zircon growth. Allanite cores and zircon mantles grew at c. 19 ± 2 and 17–15.5 Ma respectively, linked texturally and chemically to the high-pressure evolution. Symplectitic rims on embayed allanite cores, wholly symplectized Aln–Ilm and Aln–Cpx grains, and high U zircon rims grew at c. 15.5–14.5 Ma, linked chemically to the presence of melt and lower pressure, high-temperature conditions. A single garnet Lu–Hf date is interpreted as geologically meaningless, with the bulk rock composition modified by melt infiltration after garnet formation. The open system evolution of these rocks precludes precise determination of the reactive bulk composition during metamorphic evolution and thus absolute conditions, especially during the early high-pressure evolution. Despite these limitations, we show that combined geochemical and petrographic datasets are still able to provide insights into the rates and timescales of deep orogenic processes. The data suggest a younger and shallower evolution for the NW Bhutan metabasites compared to similar rocks in the central and eastern Himalayas.

1 | INTRODUCTION

Deciphering the evolution of continental collisional belts through time relies on constraining pressure–temperature–time (P–T–t) paths of metamorphic rocks to determine changing conditions throughout the orogen at different times. Determining accurate and precise P–T–t paths in turn requires linking absolute and relative geological ages to specific metamorphic conditions (e.g. Engi, 2017; Kohn et al., 2017; Mottram et al., 2014; Regis et al., 2016; Rubatto et al., 2011). In high-temperature metamorphic terranes, major and trace elemental/isotopic datasets have increasingly been found to be decoupled in the major rock-forming minerals, due to differential element diffusion (e.g. Kunz et al., 2018; Kusiak et al., 2013). Furthermore, open system behaviour, such as the loss or infiltration of fluids or melt, changes the effective bulk composition at different stages of the metamorphic evolution. These processes complicate being able to link the major and accessory phase petrographic and geochemical records with certainty, as well as hindering the determination of precise constraints on the prograde metamorphic history. However, such rocks still preserve important information that allows the metamorphic and tectonic evolution of an area to be unravelled, particularly when combining geochemical and petrographic observations.

The Himalayan orogen, formed over the last 50 Ma during the collision between the Indian and Asian continents, is the largest active continental collision zone on Earth. The metamorphic core of the orogen, represented by the Greater Himalayan Sequence (GHS) is lithologically dominated by metapelites that generally record a medium-pressure, medium-temperature history (e.g. Robyr et al., 2023). In the central and eastern Himalaya (Ama Drime, Sikkim and Bhutan) isolated metabasaltic rocks exposed at the highest structural levels of the GHS instead record a higher pressure (plagioclase-absent) to higher temperature (orthopyroxene-present) evolution (Corrie et al., 2010; Cottle et al., 2009; Groppo et al., 2007; Grujic et al., 2011; Kali et al., 2010; Kellett et al., 2014; Liu et al., 2007; Lombardo & Rolfo, 2000; Regis et al., 2014; Rolfo et al., 2008; Wang et al., 2017; Warren et al., 2011). These rocks (commonly called granulitized eclogites in the literature) have been interpreted as recording the evolution of the deeper orogenic crust during the later stages of collision, but their pressure–temperature–time evolution and the geodynamic implication are still debated (e.g. O'Brien, 2019).

Most of the geochronological evolution of the central and eastern Himalayan granulitized eclogites has been determined from zircon, with additional information from rutile and garnet. Zircon ($ZrSiO_4$) is an important petrochronological mineral in high-grade metamorphic rocks (Rubatto, 2017), as it hosts suitable concentrations of elements that record time (U, Th), temperature (Ti) and co-existence of other phases such as garnet (Y and REE). Chemical zoning that allows different crystallization episodes to be distinguished is also commonly discernible through cathodoluminescence (CL) imaging. Zircon, however, is relatively unreactive compared to other geochronometers such as monazite, and may only grow during metamorphism in the presence of fluids (Rubatto, 2017).

The interpretation of zircon U–Pb isotope data as dating the age of formation of the high-pressure (eclogite facies) assemblage and/or its replacement by a high-temperature (granulite facies) assemblage during decompression is still debated. Zircon with weak negative Eu anomalies in mafic rocks has been interpreted as recording the timing of growth in a feldspar-free reaction volume between 15.3 ± 0.3–14.4 ± 0.3 Ma in NW Bhutan (Grujic et al., 2011) and 14.9 ± 0.7–13.9 ± 1.2 Ma in the Dinggye region of the Ama Drime Massif (Wang et al., 2017). Older evidence for high-pressure metamorphism in the Ama Drime Massif has been suggested by U–Pb dating of monazite and zircon cores in felsic rocks at c. 30–29 Ma (Wang et al., 2021) and Lu–Hf dating of garnet in mafic rocks in Ama Drime at 20.7 ± 0.4 Ma (Corrie et al., 2010) and 37–34 Ma (Kellett et al., 2014).

Zircon rim dates in mafic rocks have alternatively been interpreted as recording the timing of crystallization of the lower pressure, higher temperature mineral assemblage. Zircon rims in Ama Drime have yielded dates of 17.6 ± 0.3 Ma (Li et al., 2003) and between 14 and 13 ± 1 Ma (Kellett et al., 2014; Lombardo et al., 2016) in different samples. Dates from monazite in the metasedimentary host gneisses have also been linked to the growth of the high-temperature assemblage. In NW Bhutan, monazites in the metasedimentary rocks hosting the mafic boudins yield LA-ICP-MS U–Pb dates between 15.4 ± 0.8–13.4 ± 0.5 Ma, that is, overlapping the bulk of published metabasite zircon dates (Warren et al., 2011). Monazite and xenotime in the Ama Drime host metapelites yield dates between 21 and 19 Ma (Wang et al., 2017) and 14 and 12 Ma (Cottle et al., 2009) in different samples. Other researchers, however, have attributed similar dates in Ama Drime to the final crystallization of decompression-related melts at

temperatures <650°C (Groppo et al., 2007; Kali et al., 2010; Wang et al., 2021, 2017). In summary, there is still considerable uncertainty about how to link the plethora of zircon, monazite and garnet dates from central and eastern Himalayan metabasites and host gneisses to P–T conditions and hence to tectonic evolution.

Allanite ([Ca,REE,Th]$_2$[Al,Fe $^{3+}$]$_3$([SiO$_4$]$_3$OH) is a REE-bearing epidote group mineral that plays a major role in REE and actinide exchange during metamorphic evolution (Hermann, 2002; Smye et al., 2014). Although allanite is known to be stable across a broad range of bulk compositions and P–T conditions, its occurrence in metabasites is most commonly restricted to greenschist-through to eclogite facies assemblages (Engi, 2017; Franz et al., 1986; Gieré & Sorensen, 2004). Magmatic allanite occurs in mafic rocks but has not, to our knowledge, yet been reported in granulite facies metabasites. Reports of allanite preservation in high-temperature metamorphic rocks have previously been restricted to migmatitic orthogneiss compositions (Gregory et al., 2012). In the Himalayas, allanite has only been reported from relatively low-grade metapelitic samples (Catlos et al., 2000; Goswami-Banerjee & Robyr, 2015; Thakur et al., 2018). Allanite can be dated using the U-Th-Pb isotope system and may provide complementary information to zircon and monazite which are commonly more abundant in metamorphic lithologies (Catlos et al., 2000; Darling et al., 2012; El Korh, 2014; Engi, 2017; Gregory et al., 2007, 2009; Hermann, 2002; Loury et al., 2016; Smye et al., 2014).

We have discovered allanite-preserving evidence for a complex microstructural and geochemical evolution in two metabasite samples from NW Bhutan. The allanite data suggest that the cores of larger grains record growth in a plagioclase-absent (suggestive of higher pressure) assemblage, whereas the symplectitic rims and smaller grains record growth during decompression in an orthopyroxene and plagioclase-present assemblage suggestive of high temperatures and lower pressures (granulite facies). In combination with new U–Pb from zircon, and trace element data from zircon and garnet, these data document the evolution of the metabasites from higher to lower pressures at relatively high temperatures. These samples provide a clear example of allanite growth at relatively high pressures and subsequent (rare) further growth and preservation during subsequent decompression at temperatures ∼>700°C.

2 | METHODS

A detailed description of sample preparation and analytical protocols is provided in Supplementary Data S1. Polished sections of all samples were prepared and analysed at The Open University (OU), UK. Zircon-bearing samples were crushed and separated using heavy liquid separation at the

Geochronology and Tracers Facility (GTF), British Geological Survey, Keyworth, UK. Samples selected for Lu–Hf garnet analysis were crushed at the OU and then separated using heavy liquids at the GTF. Cathodoluminescence (CL) images of zircon were taken using a dual-beam FEI Quanta 3D scanning electron microscope with a Deben Centaurus Cathodoluminescence detector at the OU. Major element analyses and element maps of mineral phases were collected at the OU using a Cameca SX100 microprobe with five wavelength-dispersive spectrometers. Elemental maps were processed using the XMap Tools software package (Lanari et al., 2014).

U–(Th)–Pb isotopes were measured in zircon (grain mounts) and allanite (in-situ) at the GTF using a Nu Instruments AttoM HR sector-field single-collector inductively coupled plasma mass spectrometer (SC-ICP-MS) coupled with a New Wave Research 193UC laser ablation system fitted with a New Wave Research TV2 cell. Methods follow those previously described in Spencer et al. (2014) and Smye et al. (2014) for zircon and allanite, respectively. Individual zircon dates (^{206}Pb/^{238}U) are common-lead corrected using a ^{207}Pb-based correction with a terrestrial lead composition at 20 Ma (Stacey & Kramers, 1975), and assuming concordance. Allanite dates are based on lower intercepts on Tera–Wasserburg plots using a free regression of ratios not corrected for common Pb. Pooled dates are quoted without and with the propagation of systematic uncertainties respectively (i.e. ±α/β), following recommendations of Horstwood et al. (2016).

Lu–Hf isotopes of whole rock and dissolved garnet separates were measured at the GTF using a Thermo-Scientific Neptune Plus multi-collector ICP-MS mass spectrometer.

Trace element concentrations in garnet, zircon and allanite were analysed at the OU by LA-ICP-MS using a Photon Machines Analyte G2 193 nm excimer laser system equipped with a HelEx II 2-volume cell coupled to an Agilent 8800 ICP-MS.

Zircon crystallization temperatures were calculated using the Ti-in-zircon thermometer (Crisp et al., 2023) for pressures of 2.0, 1.5 and 1.0 GPa assuming a silica activity of 1 and TiO$_2$ activities of 1–0.6 (both quartz and rutile were present in the high-pressure assemblage, but TiO$_2$ activities may have been lower in the ilmenite-bearing high-temperature assemblage). Quoted uncertainties include combined analytical thermometer calibration uncertainties.

Thermobarometric modelling was attempted to help constrain the conditions at which the higher and lower pressure assemblages were stabilized, acknowledging that the considerable chemical re-equilibration during retrogression makes it impossible to determine what the equilibrium mineral compositions were during high-pressure evolution. Mineral assemblage changes in EWB 071 were

modelled using Theriak-Domino v.2015 (de Capitani & Petrakakis, 2010) and thermodynamic dataset ds55 (Holland & Powell, 1998; updated August 2004) adapted by D. Tinkham. The phase equilibrium models were calculated in the eleven-component system $MnO–Na_2O–CaO–K_2O–FeO–MgO–Al_2O_3–SiO_2–H_2O–TiO_2–Fe_2O_3$ (MnNCKFMASHTO).

Due to the difficulty of constraining the true reactive bulk rock composition for each metamorphic stage in these heavily symplectised metabasites (cf. Lanari & Engi, 2017), we used two different approaches for estimating bulk rock compositions (full details in Supplementary Data S1:

1. A centimetre-scale bulk composition was estimated using XRF data from the University of Leicester, taking into consideration unmodelled accessory phases such as apatite (similar to the approach used by Weller et al. (2013) and Groppo et al. (2007)).
2. A millimetre-scale bulk composition was estimated using point-counted modal mineral abundances in conjunction with recalculated molecular mineral formulae for EMPA analyses of major mineral phases.

3 | FIELD RELATIONSHIPS AND SAMPLE DESCRIPTIONS

The high-grade metabasites in NW Bhutan are exposed in metre-scale boudins hosted by migmatitic sillimanite-grade metasediments and orthogneiss at the upper structural levels of the high-grade metamorphic unit, the Greater Himalayan Sequence (GHS; Chakungal et al., 2010; Figure 1). Field and petrographic observations suggest infiltration of melt from the host rocks into the metabasites along veins and veinlets (Supplementary Data S2). The metabasites preserve petrographic evidence for a high-pressure (HP) assemblage of garnet, clinopyroxene (hereafter termed Cpx1) and quartz, heavily overprinted by a high-temperature (HT) assemblage of augitic clinopyroxene (hereafter termed Cpx2), orthopyroxene, plagioclase and hornblende (Figure 2).

Five metabasite samples (EWB 071, 063, 064, 017x and RBC; locations in Figure 1 and lat/long details in Supplementary Data S3)were selected for this study. All samples contain garnet, clinopyroxene, quartz, plagioclase, hornblende, zircon, apatite, ilmenite and magnetite. Rare allanite is additionally present in EWB 071 and 064, rutile in EWB 071, orthopyroxene and biotite in EWB 071, 017x and 064 and chalcopyrite in EWB 071 and 017x. Extensive chemical datasets of U–Pb and Lu–Hf isotopes were collected from EWB 071 zircon and garnet respectively in addition to major and trace element concentrations from those and other major rock-forming phases. These datasets are complemented by less extensive datasets from the other samples. Whole-section photographic scans are documented in Supplementary Data S2. Mineral
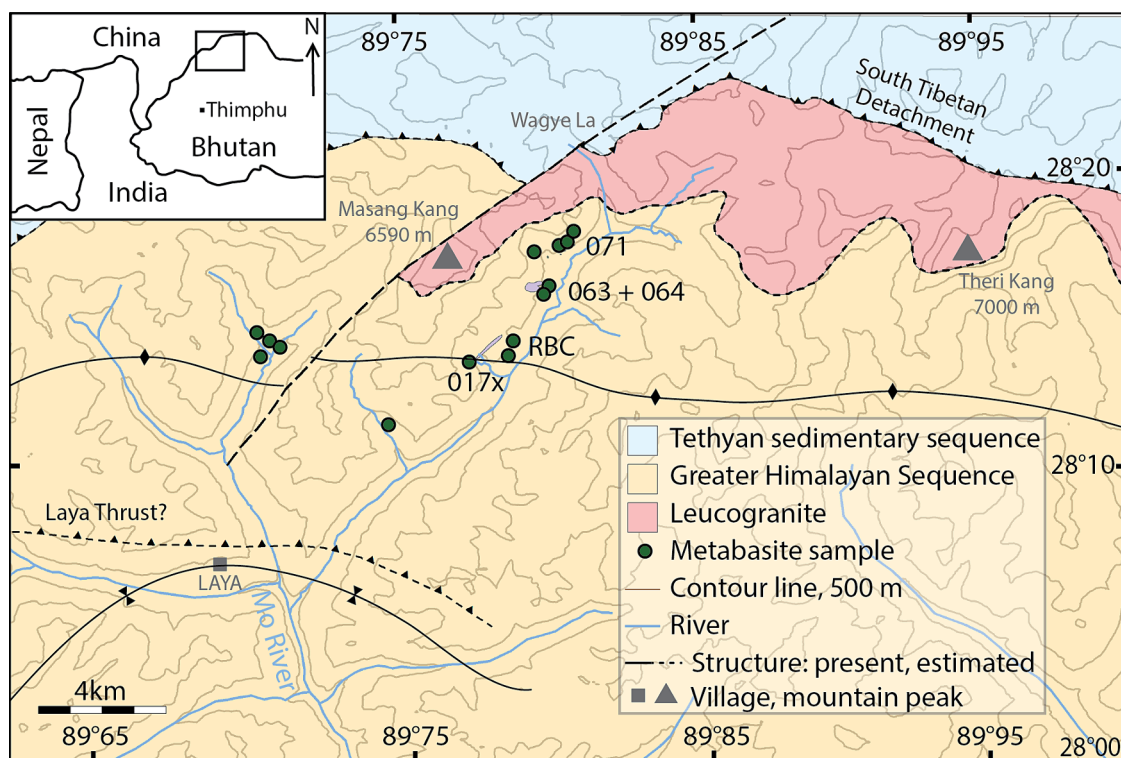
FIGURE 1 Geological sketch map of NW Bhutan showing the sampling localities for the reported samples. The inset shows the location of the study area in the eastern Himalaya.
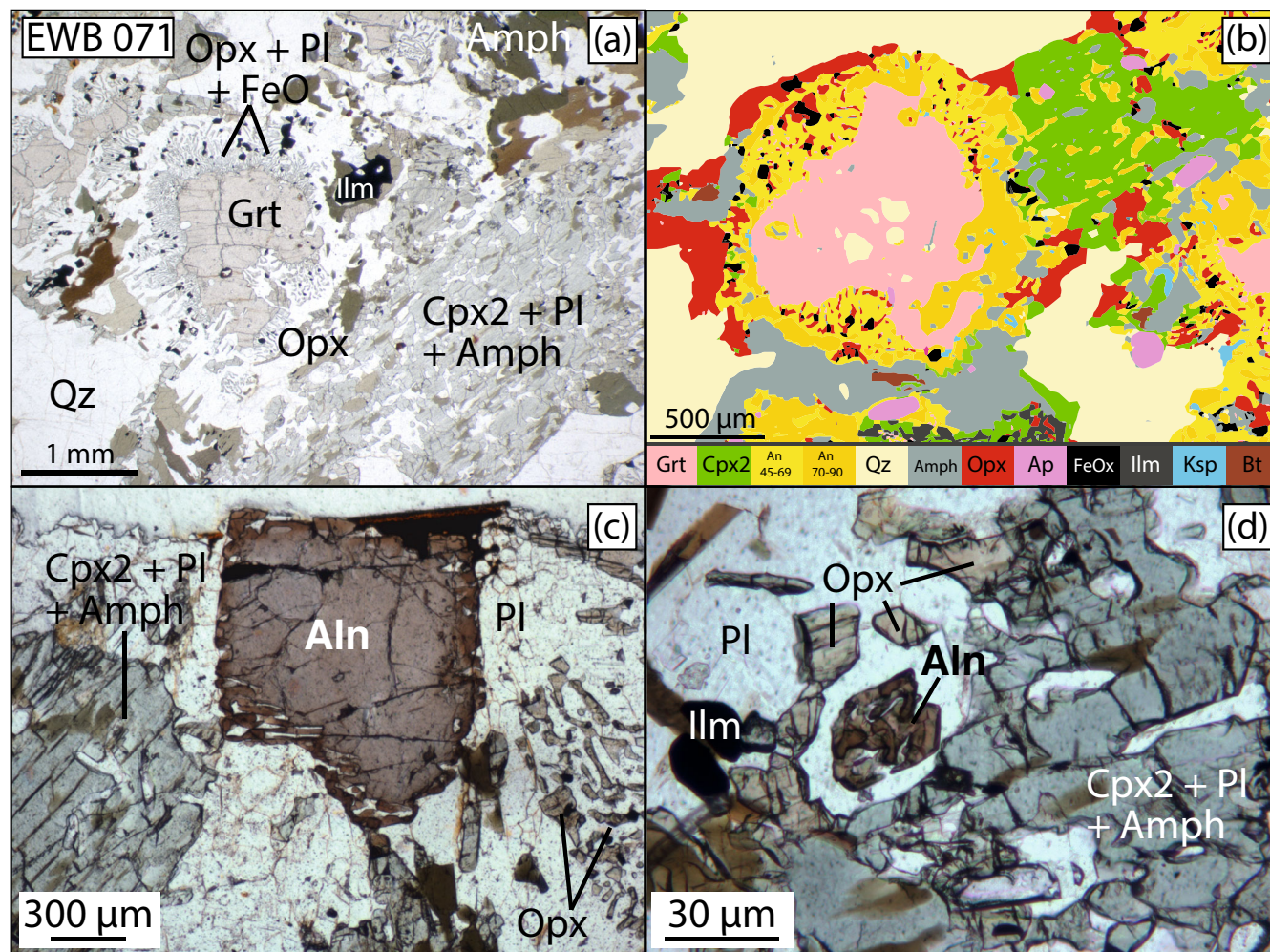
FIGURE 2 Images of sample EWB 071. (a) Overview photomicrograph showing mineralogy and textures: garnets are highly corroded and are replaced proximally by symplectites of orthopyroxene + plagioclase + magnetite, and distally (or proximally in more retrogressed domains) by amphibole + plagioclase. Symplectites of augitic clinopyroxene (Cpx2) + plagioclase + amphibole are interpreted as replacing the original Cpx1. (b) False colour mineral map produced by XMap tools (Lanari et al., 2014) showing the mineral distribution in a different area of the thin section. (c, d) Photomicrographs showing different allanite morphologies and sizes in a range of textural positions. (c) 500-μm allanite grain with dark vermicular rims intergrown with plagioclase feldspar. (d) Prismatic symplectised allanite grain intergrown with clinopyroxene (Cpx2) in association with orthopyroxene and plagioclase.

abbreviations follow Whitney and Evans (2010) throughout the text.

3.1 | EWB 071

Sample EWB 071 (Figure 2 and Supplementary Data S2) was collected from the same boudin as sample BH219 reported by Chakungal et al., 2010, and reported by them as forming from a tholeiitic basalt protolith. It is compositionally domainal on a centimetre scale, with variations in both the modal proportions of mafic (Grt, Cpx and Hbl) and felsic (Qz, Pl ± Ksp) minerals and the progression of the retrogressive overprint of the more mafic domains. The domain boundaries between more mafic and more felsic domains are diffuse.

The more mafic domains originally contained garnet (~30%–40% by volume), clinopyroxene (30%–40% by volume) and quartz. Both the garnet and clinopyroxene are now highly corroded. Subhedral almandine garnets ($Alm_{0.56–0.65}Grs_{0.19–0.33}Pyr_{0.08–0.21}Sps_{0.01–0.06}$), broadly show flat major element zoning, with minor core enrichment in Mg and Mn (Figure 3a). Inclusions in garnet are primarily quartz, with minor biotite, zircon, magnetite, apatite and rutile. Embayed grain boundaries are rimmed by fine-grained symplectites of ferrosilite orthopyroxene ($X_{Mg}0.37–0.42$) + calcic
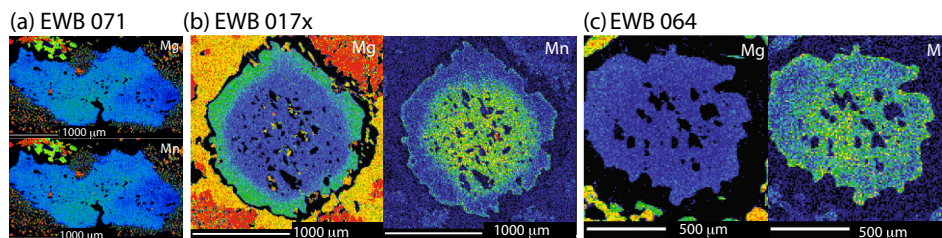
FIGURE 3 Electron microprobe maps of mg and Mn concentrations in garnets. (a) EWB 071, (b) EWB 017x and (c) EWB 064. The intensities are scaled identically across the grains (blues = low concentration, reds = high).
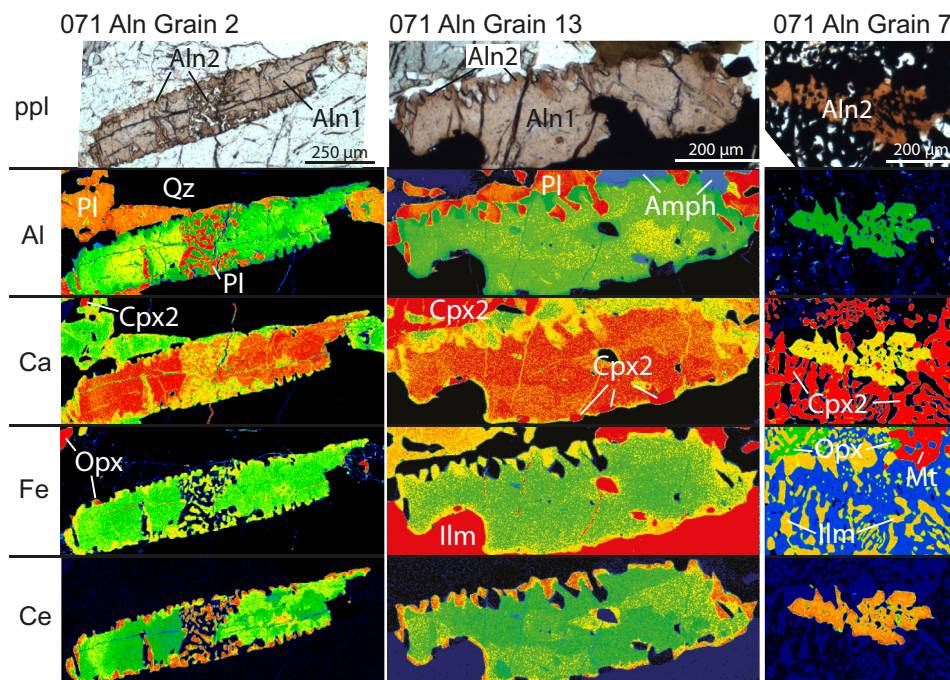
FIGURE 4 False colour X-ray element maps of typical allanite grains 2, 13 and 7 in EWB 071. The intensities are scaled identically across the grains (blues = low concentration, reds = high). Note the Ca, Fe and Ce concentrations in grain 7 are similar to the concentrations in the rims of grains 2 and 13 (both considered Aln2). Ppl, plane polarized light.

plagioclase ($An_{0.60–0.86}$) ± magnetite ± apatite. Coarser symplectites of calcic amphibole (ferropargasite, Leake, 1978) + more sodic plagioclase ($An_{0.55–0.61}$) are present more distally from garnet and completely replace orthopyroxene symplectites in more retrogressed portions of the sample. Granular orthopyroxene separates former garnet (or the replacement Opx + Pl or Hbl + Pl symplectites) from quartz (Figure 2a,b).

Symplectitic intergrowths of optically continuous augitic clinopyroxene (Cpx2; X_{Mg}0.50–0.55) and sodic plagioclase ($An_{0.46–0.74}$) with minor interstitial hornblende (Figure 2a,b) are interpreted as having grown in replacement of an original clinopyroxene, Cpx1. More retrogressed regions of the sample contain higher proportions, and larger grains of, calcic amphibole, which shows little compositional variation (X_{Mg}0.35–0.39).

Allanite occurs in a range of textural contexts in EWB 071, including within the matrix Cpx2 + Pl assemblage, at the margins of Qz–Fsp assemblages (interpreted as

infiltrated melt) and intergrown with Ilm + Cpx2 (Figure 2c,d). Tabular or prismatic grains between 0.1–2 mm in length are present in both mafic and felsic domains. Larger grains contain pale pink, faintly pleochroic cores (Aln1) and darker brown 10–50-µm-wide rims (Aln2) (Figure 2c; Figure 4). Rare rutile inclusions are present in Aln1. Aln1–Aln2 boundaries are irregular. Aln2 rims are discontinuous and commonly infill shallow embayments around Aln1 cores. Lobate embayments containing ilmenite, Cpx2 and optically continuous anorthitic plagioclase penetrate both Aln2 and Aln1 zones of larger (up to 1 mm wide) grains (Figure 2c; Figure 4, grain 13). Aln2 is present in three petrographic associations: intergrown with anorthite in a symplectite texture on the rims and fracture zones of the large Aln1 porphyroblasts (Figure 2c; Figure 4, grain 2) or intergrown in a symplectite texture with either anorthite, ilmenite or Cpx2 in smaller individual grains (Figure 2d; Figure 4, grain 7).
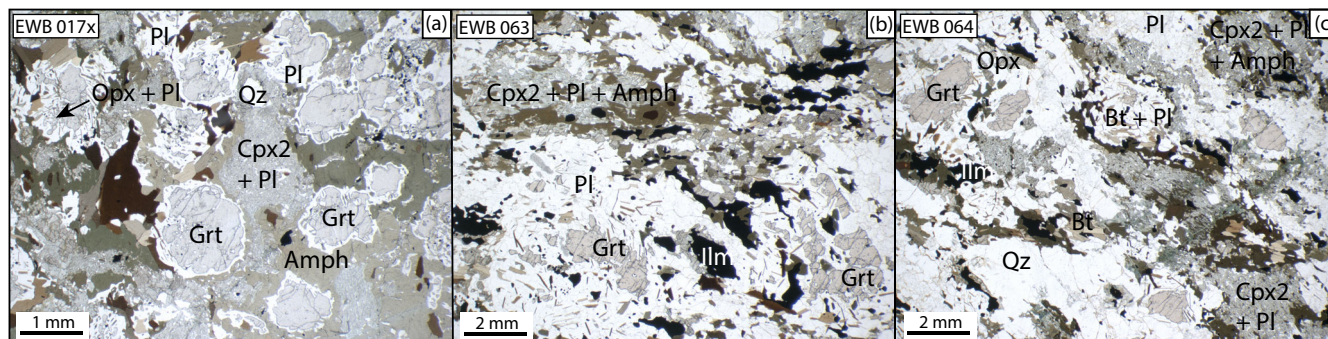
FIGURE 5 Photomicrographs of samples EWB017x (a), 063 (b) and 064 (c) in plane polarized light.

Zircon is sparsely distributed and is present as inclusions in garnet, in biotite and along grain boundaries. Apatite grains up to 300 μm in length (Figure 2b) are distributed throughout the matrix, commonly in association with mafic domains including the Cpx2 + Pl symplectites. Some apatite grains contain inclusions of Cpx2. Rutile is present in allanite and garnet cores, whereas ilmenite is present only in the matrix. Ilmenite grains are commonly rimmed by orthopyroxene and are associated with chalcopyrite and magnetite.

3.2 | EWB 017x

Sample EWB 017x is a coarse-grained, relatively undeformed metabasite (Figure 5a, Supplementary Data S2). Garnet forms roughly equant idiomorphic grains that vary from appearing relatively intact to being nearly completely replaced and record a clear variation in composition between core and rim ($Alm_{0.53–0.54}$ $Grs_{0.26–0.33}$ $Pyr_{0.11–0.19}$ $Sps_{0.01–0.04}$, Figure 3b). Garnet cores contain a higher density and variety of inclusions (quartz, amphibole, ilmenite, clinopyroxene, zircon and plagioclase) than the rims (apatite and zircon). In many instances, the cores have been preferentially replaced compared to the rims, leaving atoll structures. Garnet is replaced by symplectites of zoned plagioclase ($An_{0.82–0.25}$), vermicular orthopyroxene ($X_{Mg}0.34–0.42$) and granular magnetite, themselves being later replaced by intergrowths of calcic amphibole (ferropargasite, Leake, 1978) and plagioclase ($An_{0.3–0.22}$). Amphibole grains exhibit a subparallel orientation.

Symplectites of Cpx2 ($X_{Mg}0.43–0.52$) + plagioclase, interpreted as replacing Cpx1, are in places further mantled by granular orthopyroxene. Millimetre-scale biotite laths are intergrown with garnet and pyroxene; many grains have been replaced by amphibole and plagioclase at their rims. Quartz is a minor component and is found predominantly as inclusions in garnet.

3.3 | EWB 063, 064 and RBC

Samples EWB 063, 064 and RBC are mineralogically similar, medium-grained, lightly foliated metabasites (Figures 5b,c, Supplementary Data S2). In the more mafic (garnet + clinopyroxene) domains, remnant garnet cores containing quartz inclusions are surrounded by granular plagioclase + biotite or plagioclase + amphibole coronas; in some places, no garnet remains. Rarely, in EWB 064, orthopyroxene ($X_{Mg}0.36$) exists as a former coronitic structure separating the original garnet from quartz (Figure 5c). A symplectite of augitic clinopyroxene Cpx2 ($X_{Mg}0.5–0.51$) and plagioclase ($An_{0.38–0.51}$), some of which has later been replaced by calcic amphibole, is interpreted to have replaced the original clinopyroxene, Cpx1. Patches of coarse myrmekite are present along grain boundaries in the mafic domains.

The more felsic domains, which have diffused boundaries to the more mafic domains, contain quartz, plagioclase and K-feldspar. Plagioclase grains with lamellar twinning are rimmed by radiating fine vermicular myrmekites and perthites. Patches of myrmekite share lobate grain boundaries with larger K-feldspar grains.

In sample EWB 064 rare allanite, typically tens of micrometres in length, dark brown and faintly pleochroic, is associated with a myrmekitic vein cutting through the sample (visible in the whole thin section photograph in Supplementary Data S2). Allanite rims are embayed and intergrown with anorthitic plagioclase (similar to EWB 071 Aln2, Figure 2d and Figure 4).

4 | RESULTS

Major element data collected from all major phases are reported in Supplementary Data S3. The trace element concentrations determined by LA-ICP-MS are reported in

Supplementary Data S4. The full geochronology datasets are reported in Supplementary Data S5. The thermobarometric modelling results are reported in Supplementary Data S6. All geochronology data are plotted using IsoplotR (Vermeesch, 2018).

4.1 | Allanite

Chemical maps generated by electron microprobe and LA-ICP-MS spot data show that allanite in EWB 071 records two distinct chemical domains (Figure 4). Large (>100 μm) grains (e.g. grain 2 in Figure 4) preserve a patchy, relatively Ca-, Al-enriched, core (Aln1) and a relatively REE-, Th-, Fe-, Mg- and Ti-enriched rim (Aln2; Table 1). Smaller grains consisting of Aln + Pl symplectites and grains preserved in ilmenite + clinopyroxene symplectites (e.g. grain 7 in Figure 4) consist entirely of Aln2. Aln1 records lower LREE concentrations, overall lower HREE concentrations, and smaller $Eu_N/Eu*_N$ (0.64–0.98; average 0.85; Figure 6a) compared to Aln2 (0.28–0.56; average 0.44).

Thirty-two U–(Th)–Pb spots on the two different chemical and textural zones across seven allanite grains

TABLE 1 Allanite major element data.

Table 1 average EWB 071 allanite compositions		
	Av core Wt%	Av rim Wt%
Number of analyses	43	29
SiO_2	33.21	31.51
Al_2O_3	19.92	16.54
TiO_2	0.37	0.69
Fe_2O_3	12.35	13.97
MnO	0.09	0.12
MgO	0.69	0.95
CaO	15.46	12.03
Y_2O_3	0.02	0.04
La_2O_3	2.98	4.76
Ce_2O_3	6.91	10.26
Pr_2O_3	1.09	1.50
Nd_2O_3	2.59	3.38
Sm_2O_3	0.31	0.34
Gd_2O_3	0.00	0.00
ThO_2	0.92	2.05
UO_2	0.10	0.10
Total	97.01	98.22

in sample EWB 071 yield two overlapping but distinct populations. The spots in Aln1 (mostly cores, Figure 6b) yield a lower intercept date of 19.2 ± 1.8/2.0 Ma (MSWD 2; uncertainties are quotes with and without the systematic uncertainties, respectively, see Supplementary Data S1). The spots in Aln2 zones (mostly rims, some symplectised grains; Figure 6c) yield a lower intercept date of 14.3 ± 0.3/0.7 Ma (MSWD 1.4). The MSWDs of these pooled dates suggest an age spread within each population; the uncertainty on each calculated date takes the MSWD into account (Vermeesch, 2020). Aln1 is generally richer in common Pb than Aln2 and the high common Pb contents of both allanite populations preclude the calculation of meaningful $^{206}Pb/^{238}U$ dates for each individual spot.
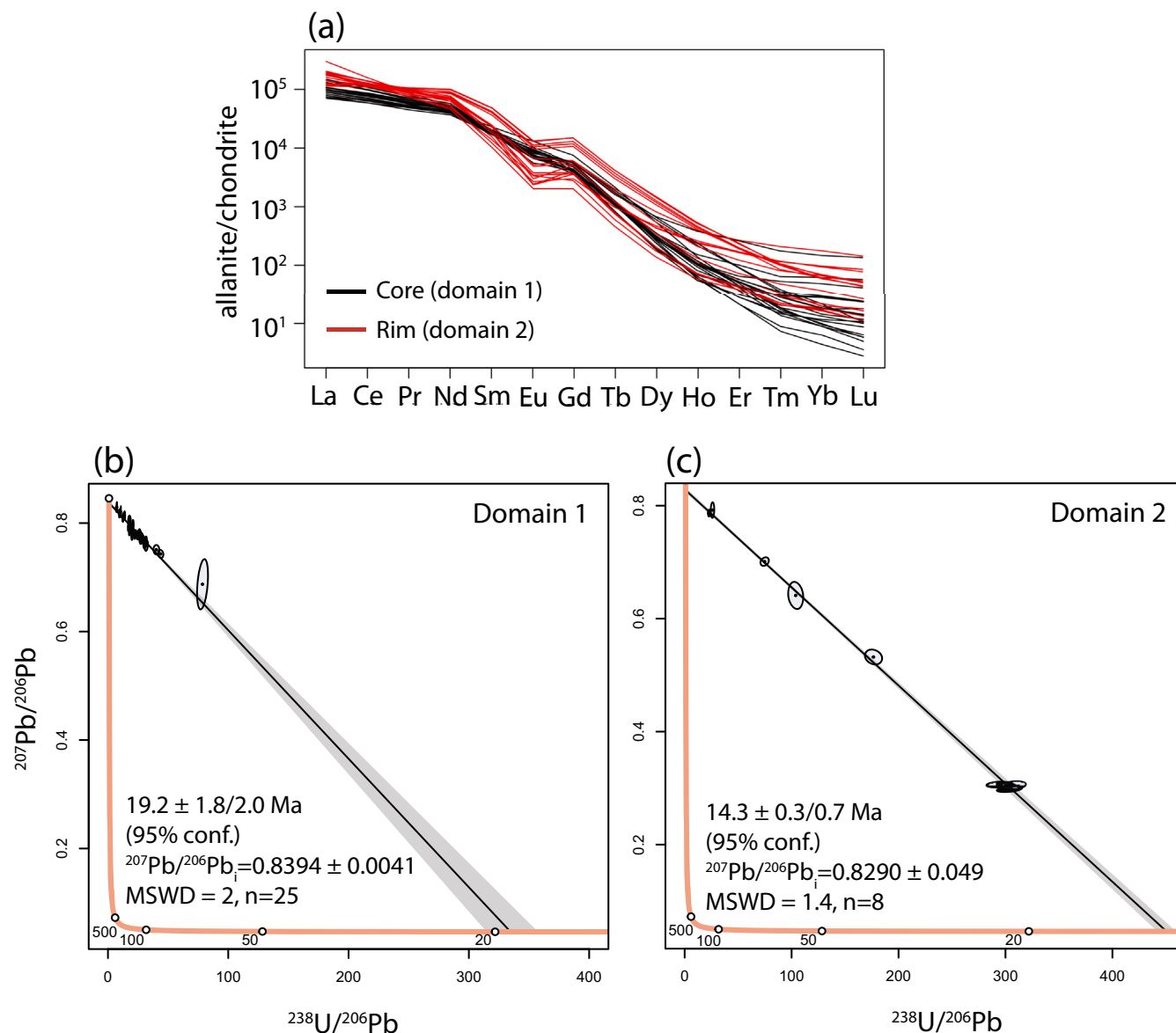
4.2 | Zircon

Zircon in all samples is present as inclusions in matrix-forming minerals and along grain boundaries. All analyses were collected from mineral separates, due to the paucity of suitable zircon in individual thin sections. Zircon grains are rounded, with elongate to soccer ball aspect ratios. Many grains exhibited high-contrast (CL-bright and CL-dark) irregularly zoned cores that yielded pre-Himalayan dates (Inh. Core; Figures 7a and 8a,b). Himalayan-aged zones typically exhibit relatively low CL-contrast, however, in sample EWB 071 higher contrast Himalayan-aged near-homogenous CL-bright (Zrn1) and CL-dark (Zrn2) zones form two rims (<5 to >50 μm wide) on inherited cores. Grains that do not have inherited cores show similar CL responses to the two Himalayan-ages rims (Figures 7a and 8a,b). Some grains exhibit sector zoning, foe example grain 064–01 (Figure 8a).

Thirty-nine spots on zircon rims in EWB 71 yielded common-Pb-corrected $^{206}Pb/^{238}U$ dates between 17.3 ± 1.2–14.6 ± 0.3 Ma (Figure 7b, Supplementary Data S5). Like the allanite dataset (and other zircon datasets presented below), the range of dates is statistically inconsistent with a single population. Low common Pb contents allow meaningful individual $^{206}Pb/^{238}U$ dates to be calculated so the dates are presented here as ranges rather than a weighted mean or pooled intercept. In this sample, different CL responses in Himalayan-aged zones match onto variations in U concentration and date. CL-bright zircon (Zrn1) contained lower U concentrations (~80–600 ppm, Figure 7b) and a higher fraction of common Pb, and yielded older dates (17.3 ± 1.2 to 15.3 ± 0.4 Ma). CL-dark zircon (Zrn2) contained higher U (~800–2000 ppm, Figure 7b) and a lower common Pb fraction and yielded a younger, but overlapping, population of

—WILEY | 775

FIGURE 6 (a) Chondrite-normalized rare earth element plot for the allanite cores (Aln1) and rims or symplectized whole grains (Aln2). (b, c) U–Pb Tera–Wasserburg plots showing the dates obtained for allanite domains. Quoted uncertainties are $\pm$ α/β, where α = analytical only, and β includes systematic components. Error ellipses are 2σ. The three analyses with the lowest common Pb concentrations in C were measured on grain 7 (Figure 4) forming an intergrowth with ilmenite and clinopyroxene.

dates (15.5 ± 0.3 to 14.6 ± 0.3 Ma). Seventy-one U–Pb zircon core analyses yielded a discordia array between 478.4 ± 16.5 Ma and c. 15 Ma (not plotted but presented in Supplementary Data S5).

Chondrite-normalized REE patterns for Himalayan-aged (<30 Ma) zircon in sample EWB 071 (Figure 7c) show a positive Ce anomaly and a flat HREE profile. Eu_N/Eu^*_N values lie in the range 0.73–1.02. Zrn1 zones yielded the highest Eu_N/Eu^*_N (0.99–1.02, Figure 7d). Ti concentrations are low, between 2 and 8 ppm, and there is no correlation between Ti concentration and age or U concentration.

Thirty-two spots on zircon rims in sample EWB 017x (Figure 8a) yielded $^{206}Pb/^{238}U$ dates between 25.4 ± 1.8–13.5 ± 0.7 Ma (Figure 8c), with all but four analyses yielding a cluster of dates between 17.5 ± 1.8–13.5 ± 0.7 Ma. Analyses older than c. 15.5 Ma show less variability in U concentration and concentrations <150 ppm, whereas analyses younger than c. 15.5 Ma have U concentrations between 69 and 245 ppm (isotope dataset). There is no obvious correlation between U concentration and CL brightness. Chondrite-normalized REE patterns for <30 Ma zircon (Figure 8g) show a positive Ce anomaly and a flat HREE profile. Eu_N/Eu^*_N values are in the
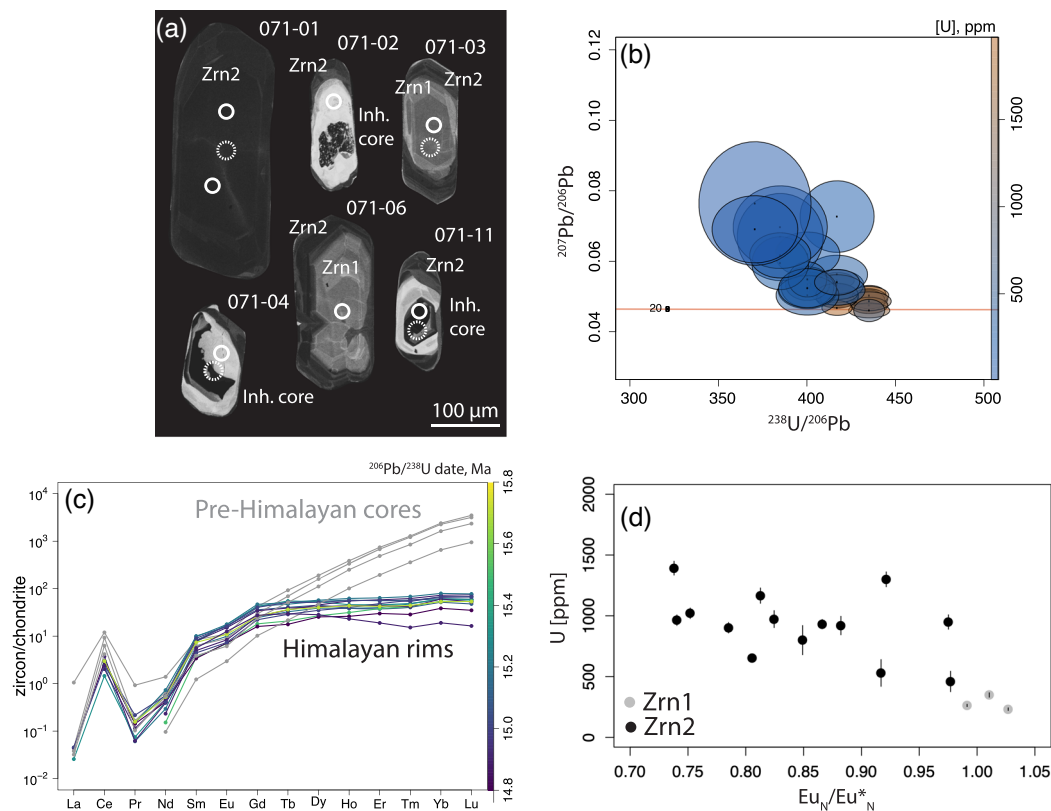
FIGURE 7 Zircon data from sample EWB 071. (a) Representative CL images of zircon grains. Solid spots represent the U-Th-Pb analyses; dashed spots indicate the trace element analyses. Inh. core = inherited core. (b) Tera–Wasserburg U–Pb plot with analyses coloured by U concentration (U data from U–Th–Pb analytical dataset). Younger grains contain higher U concentrations. Error ellipses are 2σ. (c) Chondrite-normalized rare earth element plot with Himalayan-aged zones coloured by $^{206}Pb/^{238}U$ age. (d) U concentrations vs. Eu_N/Eu^*_N for CL-bright Zrn1 (dark grey) and CL-dark Zrn2 (pale grey) (U data from trace element dataset, not the isotope dataset).

range 0.83–1.24. Ti concentrations are low, between 2.3–7.6 ± 0.6–1.7 ppm.

Twenty-nine spots on zircon rims in sample EWB 064 (Figure 7d) yielded $^{206}Pb/^{238}U$ dates between 22.8 ± 2.6–9.7 ± 1.0 Ma. Eu_N/Eu^*_N values vary from 0.92–1.32 and Ti concentrations from 1.4–4.2 ± 0.4–0.8 ppm. Spots older than 15 Ma have U concentrations <100 ppm, whereas spots younger than 15 Ma have U concentrations from 8 to 140 ppm.

Twenty-one spots on zircon rims in sample EWB 063 (Figure 7e) yielded $^{206}Pb/^{238}U$ dates between 16.3 ± 0.6–13.3 ± 0.4 Ma. Forty-seven spots on zircon rims in sample EWB RBC (Figure 7f) yielded $^{206}Pb/^{238}U$ dates between 17.4 ± 1.3–13.2 ± 1.0 Ma.

4.3 | Garnet

Garnet major element compositions are similar between samples and fairly homogeneous across grains. Garnets are almandine-rich: ~55%–60% almandine, 25%–30%

grossular, 10%–20% pyrope and minor spessartine (Supplementary Data S2, Figure 3).

Garnets in samples EWB 071, 017x and 064 show flattened HREE patterns and, generally a lack of, or small, Eu anomaly (Eu_N/Eu^*_N 0.63–1.48) (Figure 9b,d,f). Gd (MREE) concentrations range from 17.7–1.9, 13.5–0.7 and 19.8–5.7 ppm, respectively, in samples EWB 071, 017x and 064, respectively (Supplementary Data S4). Lu (HREE) concentrations range from 2.4–0.4, 2.7–0.01 and 4.4–0.7 ppm in samples EWB 071, 017x and 064, respectively (Supplementary Data S4). HREE and Y concentrations in EWB 071 and 064 increase from (geometric) core to (current remaining) rim. Garnets in samples EWB 071 and 064 record only minor core–rim changes in REE concentrations.

Two aliquots of garnet and bulk rock from sample EWB 064 yielded a Lu–Hf isochron that provided a date of 15.3 ± 0.3 Ma (2 s), MSWD 3.5 (Figure 10). Lu–Hf isotopes measured in garnets from samples EWB071 and EWB17x failed to produce an isochron. These data are presented in Supplementary Data S5.
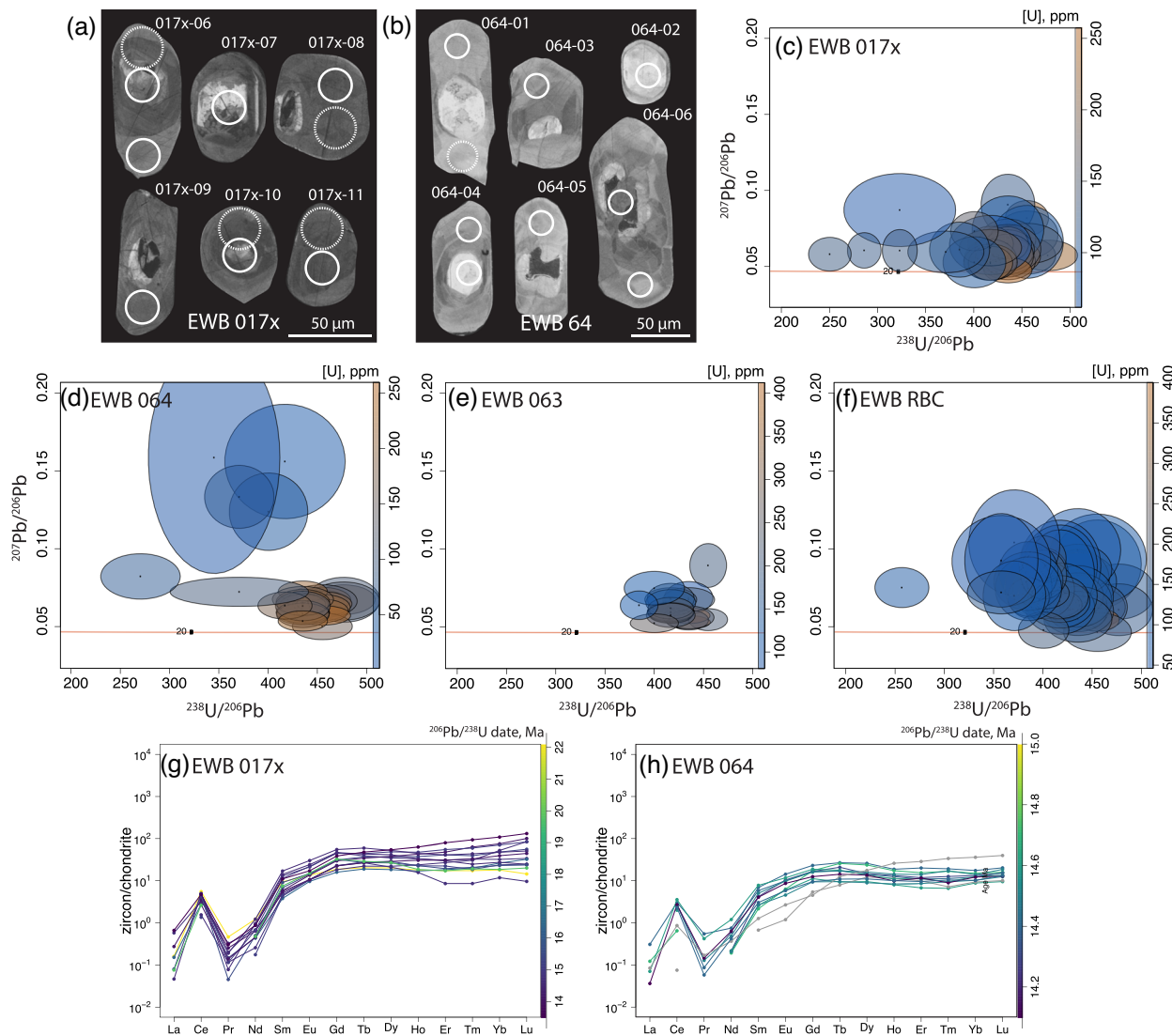
FIGURE 8 Zircon data for samples EWB 017x, 064, 063 and RBC. (a, b) Representative CL images of zircon grains from samples EWB 017x and 064. Solid spots represent the U–Th–Pb analyses; dashed spots indicate the trace element analyses. (c–f) Tera–Wasserburg U–Pb plot with analyses coloured by U concentration; note the difference in U concentration scale between (c, d) and (e, f). Error ellipses are 2σ. (g, h) Chondrite-normalized rare earth element plots for samples EWB 017x and 064 with Himalayan-aged zones coloured by $^{206}Pb/^{238}U$ age.

4.4 | Pressure–temperature determinations

Ti-in-zircon thermometry for Ti concentrations in the Himalayan-aged zircon at $P = 1.5$ GPa and TiO$_2$ activity of 1 vary from 630 to 740°C in EWB 071 (with no difference between Zrn1 and Zrn2), 640–740°C in EWB 017x and 600–680°C in EWB 064 (all with calibration uncertainties of ±80–100°C, Crisp et al., 2023). At $P = 2$ GPa, calculated temperatures are ~20°C higher. At $P = 1$ GPa, calculated temperatures are ~15°C lower. Under low-pressure conditions where ilmenite is the only Ti-bearing phase in the assemblage, TiO$_2$ activity may be reduced to 0.9–0.6 (Ferry & Watson, 2007). A reduction in activity to

0.6 at 1.0 GPa increases the calculated temperatures by ~40°C compared to an activity of 1 at the same pressure (Supplementary Data S4).

The aim of the thermobarometric modelling was to help constrain the conditions at which the higher and lower pressure assemblages were stabilized, as the pressure path in particular has implications for the tectonic evolution of the region. The pseudosections calculated for the two different bulk compositions (Supplementary Data S6) show different results, especially in the position of the (dis)appearance of pressure-dependent phases such as plagioclase and rutile.

The higher pressure conditions are characterized mineralogically by the presence of rutile and clinopyroxene1

EWB 071

EWB 17x

EWB 064
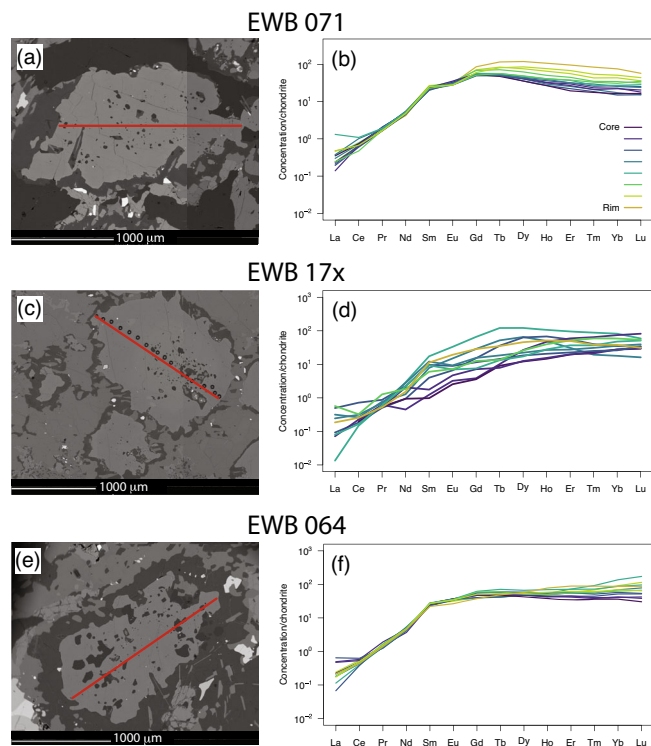
FIGURE 9 Garnet backscatter electron images (a, c, e) and trace element data (b, d, f) for samples EWB 071, 017x and 064. Figures a, c and e show the profiles along which the trace element data were collected (spots shown in c).

(6.5% Jd) and the absence of plagioclase, orthopyroxene and clinopyroxene2 (augite). Rutile-present, plagioclase-absent conditions with 6.5% jadeite are estimated at a lower P limit of >1–1.5 GPa (centimetre-scale bulk) and >1.5–1.7 GPa (millimetre-scale bulk) and below the solidus. However, it is worth noting that the rutile stability is extremely sensitive to bulk composition and varies by 0.5 GPa between the two estimates.

The lower pressure conditions are characterized mineralogically by an assemblage of Grt–Pl–Opx–Cpx(2)–Qtz–Ilm ± Hbl. The millimetre-scale and centimetre-scale pseudosections predict this assemblage, albeit without hornblende, to be stable below 0.7 GPa.

5 | DISCUSSION

Petrographic, isotopic and elemental data from different chemical zones in allanite and zircon in NW Bhutan metabasite samples record evidence for two main phases of crystallization under higher pressure (plagioclase-absent, rutile-present) between c. 19.0–15.5 Ma and lower pressure but high-temperature (plagioclase- and orthopyroxene-present) conditions between c. 15.5 and 14.5 Ma.

The complex symplectite relationships and the thermal re-equilibration of the major element chemistry of the rock-forming phases in the metabasite samples make it impossible to determine the reactive bulk rock composition for the high-pressure stage with any accuracy. This in turn restricts the calculation of any meaningful P–T–t paths. Regardless, the recognition of two chemically and petrographically distinct allanite zones plus the recognition of two chemically distinct zircon zones provide new observations to fit into the relative sequence of mineral reaction. Together with the geochronological data, these observations shed new light on key parts of the metamorphic evolution of this enigmatic and deep-rooted part of the Himalayan orogen.

5.1 | Allanite

Petrographic, isotopic and elemental data show that allanite in sample EWB 071 grew in two separate episodes under different conditions. Allanite 1, which is preserved as the cores of mostly larger grains, is typified by relative Ca and Al enrichment and REE, Th, Fe, Mg and Ti depletion. The presence of rutile inclusions, the lack of a negative Eu anomaly (Eu_N/Eu^*_N) and the U–Pb data suggest that Aln1 grew in a high-pressure plagioclase-absent assemblage at 19 ± 2 Ma.

Allanite 2 always occurs within symplectite structures. It is typified by relative REE, Th, Fe, Mg and Ti enrichment and relative Ca and Al depletion compared to Aln1. The negative Eu_N/Eu^*_N, the symplectitic associations and the U–Pb data suggest that Aln2 grew during decompression at high temperatures at 14.3 ± 0.3 Ma. Previous studies suggest that allanite grains >20 μm wide retain radiogenic Pb at temperatures >700°C for >10 Ma (Gregory et al., 2012; McFarlane, 2016; Oberli et al., 2004; Smye et al., 2014) and can thus preserve evidence for growth across multiple metamorphic stages or during different metamorphic events. We therefore interpret the allanite U–Pb dates in our samples as recording the timing of allanite crystallization in both chemical domains.

The association of anorthite with Aln2 rims on large Aln1 porphyroblast cores suggests a decompressive reaction that involves Aln1 reacting to Aln2 + An (cf. Matthews & Goldsmith, 1984 who ran experiments to constrain the P–T conditions of formation of zoisite from anorthite). This reaction implies preferential partitioning of the REE + Fe released from Aln1 into Aln2 and Ca + Al into the newly-formed anorthite. The intergrowth of Aln2 with ilmenite and Cpx2 suggests Aln2 growth at pressures lower than the rutile and Cpx1 stability fields respectively (Angiboust & Harlov, 2017; Frost et al., 2001) and potentially during the breakdown of titanite

—WILEY—

FIGURE 10 Garnet Lu–Hf isochron for two aliquots of garnet anchored by two aliquots of whole rock sample EWB 064.
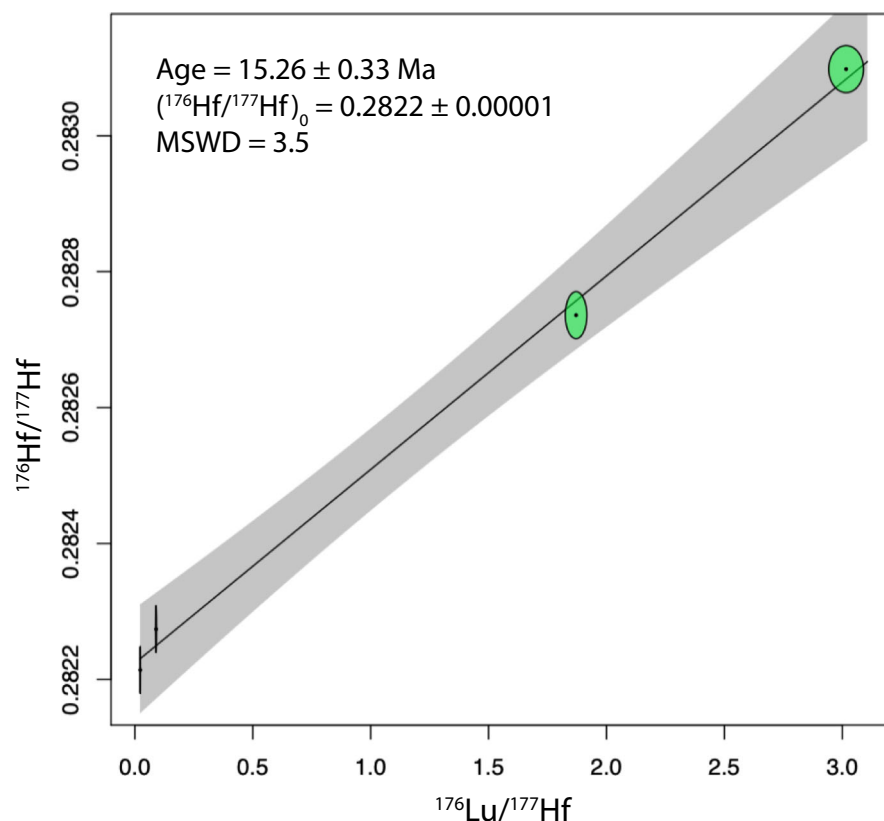
(cf. Marsh & Smye, 2017); no titanite remnants are preserved in the current assemblage.

The sequence of growth of Aln1 and Aln2 is inverse to the prograde compositional variation commonly reported in eclogites, typified by relatively REE-enriched allanite cores overgrown by relatively REE-depleted clinozoisite/epidote rims during decompression (Airaghi et al., 2019; Janots et al., 2007, 2008, 2009; Smye et al., 2011; Spear, 2010; St-Onge et al., 2013). Such inverse zoning has previously been reported only in heavily metasomatised garnet–amphibolite migmatites, with LREE-enriched rims attributed to the influx of externally derived REE-enriched fluids (Sorensen, 1991). Some of the growth of Aln2 in the NW Bhutan samples may have been connected to external fluid influx (e.g. from melt or other fluids infiltrating the boudins from the metasedimentary host rocks, for which there is field evidence). A full thin-section photograph of EWB 064 (Supplementary Data S2) shows a felsic vein with several allanite grains located at the boundary between the vein and the metabasite.

5.2 | Zircon

The chemical zoning and U–Pb dates documented in zircon provide information that complements and

supplements the allanite record. Zircon in sample EWB 071 yielded two (overlapping) populations of Himalayan-aged cores and rims (17.3 ± 1.2 to 15.3 ± 0.4 Ma and 15.5 ± 0.3 to 14.6 ± 0.3 Ma) that link to CL response and U concentration. These ranges may either imply analytical mixing between different zircon growth zones or may reflect the timescales of zircon crystallization during metamorphism. While instances of mixed zircon crystallization zone analyses cannot be totally excluded from explaining elevated U compositions in Zrn2 in some grains, grains which are solely composed of Zrn2 also yield similar high U concentrations. Zircon in samples EWB 017x and 064 also record a trend of increasing U concentrations with age from c. 15.5 Ma (Figures 7b and 8c,d, Supplementary Data S5). These trends imply either the breakdown of a U-enriched phase in these samples during zircon growth or could imply zircon growth in the presence of melt. Candidate phases for dissolution in the high-pressure assemblage include detrital/inherited zircon (the pre-Himalayan cores contain concentrations of 60–7490 ppm U), allanite (up to 0.2 weight % U), and garnet (<0.3 ppm U but volumetrically significant), all of which exhibit resorption textures. The U concentrations of apatite and rutile in these samples are unknown but could also be a potential source of U for zircon growth (Degeling et al., 2001). Textural evidence for the dissolution of pre-Himalayan zircon cores is shown by

truncation of features in the CL images by younger (Himalayan-aged) overgrowths (Figures 7a and 8a,b). However, the textural relationships between the older Zrn1 and the younger Zrn2 populations in EWB 071 do not suggest extensive dissolution between those growth episodes. A small amount of low-degree melt infiltrating the mafic boudin from the host metapelites could have brought U with it, and the presence of melt is known to facilitate zircon growth in metamorphic rocks (e.g. Rubatto, 2017; Rubatto et al., 2013). Allanite, however, exhibits significant textural evidence for dissolution following the growth of the porphyroblast cores and therefore could also be a viable source of U for Zrn2.

In EWB 071, Zrn1 and Zrn2 also have distinctive Eu concentration signatures. Zrn1 shows an Eu_N/Eu^*_N of ~1, that is, no anomaly, whereas Zrn2 shows a trend towards a more negative Eu_N/Eu^*_N (Figure 7d). These data suggest Zrn1 started to crystallize in a plagioclase-absent assemblage and Zrn2 started to crystallize in a plagioclase-present assemblage, with some overlap. Overall, the data suggest that zircon in sample EWB 071 records growth between 17.3 ± 1.2 to 15.3 ± 0.4 Ma under high-pressure conditions when zircon was not competing for Eu with plagioclase (Hinton & Upton, 1991; Murali et al., 1983; Rubatto, 2002, 2017) and between 15.5 ± 0.3 to 14.6 ± 0.3 Ma under lower pressure conditions. Given the fact that these rocks have been heavily overprinted and the chances of analytical mixing of different growth domains, we suggest that the older (17 Ma) end of the Zrn1 range is most likely to represent the timing of zircon crystallization at higher pressures. Similarly, we interpret the younger (14.5 Ma) end of the younger age range to be the most realistic estimate of the timing of zircon growth at lower pressures.

Zircon in samples EWB 017x and EWB 064 yield overlapping age populations with EWB 071, and show a similar trend in increasing U concentrations over time. However, changes in their Eu_N/Eu^*_N signatures with U concentrations or age are less clear. Their Eu_N/Eu^*_N and HREE signatures are suggestive of growth either in an assemblage where plagioclase was absent or during the transition to a plagioclase-present assemblage.

Calculated Ti-in-zircon temperatures are similar from all three samples, ranging from 630 to 740°C in samples EWB 071 and 017x and 600–680 in EWB 064 (calculated for 1.5 GPa). We did not observe any discernible difference in Ti-in-zircon temperatures for EWB 071 Zrn1 and Zrn2 (Supplementary Data S4), or correlation between temperature and U or temperature and Eu_N/Eu^*_N. The temperatures are similar to those reported in a previous study of the same region, recalculated to the same calibration (Crisp et al., 2023; Grujic et al., 2011).

5.3 | Garnet

In general, the garnet in all of the studied samples is subhedral, heavily corroded, and preserves little major element zoning (with the exception of sample EWB 017x), which makes interpreting the location of the original growth cores difficult in most samples. Garnets in sample EWB 017x preserve inconclusive REE zoning patterns; the dataset may reflect the mixing of garnet-hosted REE with REE contained in inclusions (e.g. rutile or zircon). Garnets EWB 071 G1 and 064 G4 record increasing concentrations of HREE and Y towards the currently-preserved rim, opposite to that expected for Rayleigh fractionation during growth, (e.g. Otamendi et al., 2002) or for diffusion-limited uptake of trace elements, (e.g. Skora et al., 2006). Instead, such increases are consistent with an increased supply of REE during back-diffusion associated with their release from garnet during its replacement by orthopyroxene and plagioclase (Carlson, 2012) or during the breakdown of other HREE- and Y-bearing phases such as zircon or allanite. In the latter scenario, the lack of concomitant increase in Zr or Ti towards the garnet rim could suggest a record of Y and HREE from allanite rather than zircon. The HREE + Y increase could also suggest equilibration of the garnet with melt, compare Rubatto et al., 2020—both allanite and zircon chemistry and textures, plus field evidence, suggest infiltration of melt into the mafic boudin from the host metapelite at c. 14.5 Ma.

The younger date yielded for the garnet (compared to the allanite Aln1 and zircon Zrn1 U–Pb dates) requires discussion. Garnet is expected to grow during prograde metamorphic evolution, and would therefore be expected to yield an older age. Additionally, garnets in EWB 064 are heavily corroded, and we interpret the remnants to be volumetrically skewed towards the original garnet core. In fact, garnet yields a Lu–Hf date that is more consistent with the dates calculated from Zrn2 and Aln2 (porphyroblast rims and fully symplectized grains), related to decompression and melt infiltration. The calculated isochron is to all intents and purposes a two-point isochron, pinned by the garnet composition at one end and the bulk rock at the other end. We suggest that the bulk rock composition has been modified after garnet growth by the infiltration of melt, such that the two compositions used to calculate the garnet Lu–Hf date are not in isotopic equilibrium, and form an 'errorchron' rather than an isochron (cf. Baxter et al., 2017). Late bulk composition modification may also explain why the other two samples did not yield a garnet isochron.

—WILEY—

5.4 | Pressure–temperature–time evolution

The two different calculated bulk rock compositions vary significantly, particularly in Al_2O_3, Na_2O and K_2O, which are enriched, and CaO and MgO, which are depleted, in the centimetre-scale bulk composition estimate compared to the millimetre-scale composition (Supplementary Data S1). These variations are likely due to differences in the 2D or 3D volume used to determine the bulk rock composition. The two bulk compositions yield significantly different stability fields for rutile, plagioclase and clinopyroxene (Supplementary Data S6).

The bulk rock composition that formed the high-pressure assemblage may have been modified during decompression by melt infiltration from the metasedimentary host rocks (there is field and sample evidence for late leucocratic veins and patches; Supplementary Data S2). This may have altered their bulk chemistry. Neither pseudosection predicts the formation of hornblende; however, stabilization of hornblende in the models is highly water dependent, and water may have been brought into the system via the melt, released to the host metabasites as the melt crystallized. Petrographically, hornblende is the last phase to crystallize, fitting with the observation that melt infiltration was in part responsible for creating the conditions for it to crystallize.

Overall, the XRF bulk composition will have incorporated more of the infiltrated melt, whereas the lower volume point-counted region was selected to focus on the mafic portion of the sample—while there is still evidence for chemical modification, this composition could more closely match the precursor mafic bulk and might better predict the HP conditions. However, the uncertainties in the available/effective bulk composition at both stages lead to large uncertainties in precise pressure and temperature estimates. Despite these limitations, careful petrographic investigation and detailed petrochronology have allowed higher and lower pressure stages to be recognized and dated.

5.5 | High pressure

The indicators of early high-pressure history in the NW Bhutan metabasites include the micro-textural association of Cpx1 + garnet + quartz + rutile, an absence of plagioclase and the lack of a (or weak) negative Eu/Eu* recorded in the geochronometer minerals and garnet (Figure 11). However, the chemical compositions of the major phases have equilibrated at lower pressure and higher temperature conditions and are no longer consistent with the petrographic record of the higher pressure

evolution. Similar textures have been described from metabasite samples throughout the central and eastern Himalaya (e.g. Corrie et al., 2010; Cottle et al., 2009; Groppo et al., 2007; Grujic et al., 2011; Kali et al., 2010; Liu et al., 2007; Lombardo & Rolfo, 2000; Rolfo et al., 2008; Wang et al., 2017) and in analogous terranes found in other orogenic belts (Anderson & Moecher, 2007; Möller et al., 2015; O'Brien & Rötzler, 2003). Attempts have been made to constrain their evolution using a variety of different thermobarometers and modelling methods, but the same issues of the sensitivity to the choice of equilibration volume, metamorphic overprinting and open system behaviour apply.

There are some P–T indicators which are helpful to at least partially constrain peak conditions. For example, the plagioclase in Cpx1–Cpx2 and rutile-out reactions provide some constraints on the pressure conditions; however, these are often strongly dependent on bulk rock composition (e.g. Lanari & Engi, 2017; Pereira & Storey, 2023). Reintegration of Cpx1 in samples EWB 071 and 017x yielded jadeite compositions between 6.5 and 20% (Supplementary Data S1), suggesting minimum pressures of 1 GPa (see centimetre-scale pseudosection in Supplementary Data S6). However, the Cpx2 and plagioclase compositions used to calculate Cpx1 may have been modified during the (non-isochemical breakdown) reactions (e.g. Möller, 1998; Zhao et al., 2001) and therefore provide no absolute constraint on the composition of Cpx1. Ti-in-zircon temperatures for Zrn1 provide an estimated temperature range of ~630–740°C for zircon crystallization which is considered reasonable given the other chemical and textural evidence.

5.6 | Lower pressure

The plagioclase-present, higher temperature metamorphic overprint that occurred during decompression is recorded by a suite of incomplete mineral reactions and trace element signatures. The evolution from high-pressure to low-pressure conditions is evidenced texturally and chemically by the formation of different plagioclase-containing symplectites (Figure 11):

i. Cpx2 + plagioclase ± amphibole after Cpx1, e.g. (Anderson & Moecher, 2007; Groppo et al., 2007);
ii. Aln2 + plagioclase or ilmenite or Cpx2 after Aln1 + titanite (e.g. Matthews & Goldsmith, 1984);
iii. Cpx2 + ilmenite intergrowths after titanite (e.g. Faryad et al., 2006, 2010; Marsh & Kelly, 2017; Marsh & Smye, 2017; O'Brien & Rötzler, 2003), and
iv. orthopyroxene + plagioclase + magnetite after garnet (e.g. O'Brien & Rötzler, 2003).
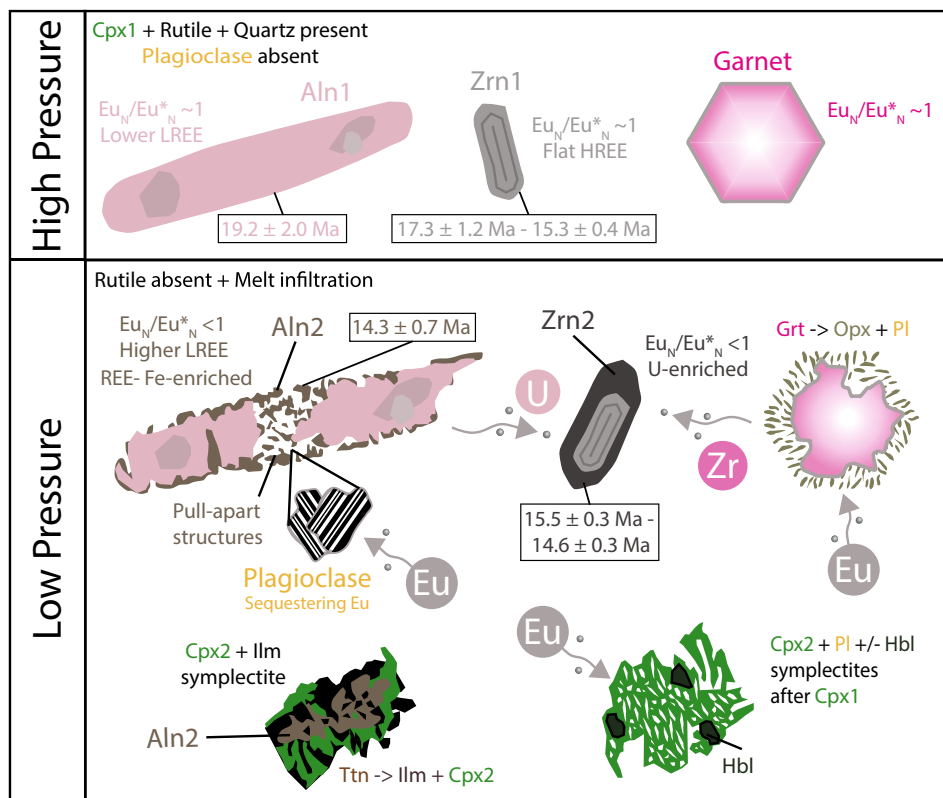
FIGURE 11 Schematic figure showing a summary of the petrographic features of the allanite, zircon garnet and symplectites in the metabasites and their relative pressure–temperature conditions of formation. The absolute pressure–temperature conditions of formation of the higher pressure assemblage are currently not possible to define precisely (see text). The formation of the symplectites suggests decompression at high temperatures (∼700–750°C, cf. Groppo et al., 2007), but open system conditions during metamorphism have altered mineral chemistry such that changes in temperature in the Bhutan samples are not currently possible to define precisely (see text).

All these symplectites, many of which are also described from metabasite samples elsewhere in the eastern Himalaya as well as globally, are suggestive of decompression at temperatures of >700°C at pressures of 0.8–1.6 GPa (cf. Anderson & Moecher, 2007). This is in general agreement with the field evidence for partial melting of the metasedimentary host rocks (muscovite dehydration melting occurs at ∼650°C in metapelites). The calculated pseudosections for EWB 071 do not provide unambiguous constraints on different reactions as the key Opx-in reaction pressures are very bulk composition dependent (Supplementary Data S6). Published pseudosections of central Himalayan samples suggest that symplectite (i) forms at the highest pressures (>1 GPa;) and symplectite (iv) at the lowest pressures (∼0.4 GPa; Groppo et al., 2007).

5.7 | Implications for Himalayan evolution

Despite the relative plethora of zircon and monazite U–Pb isotope data from 'granulitized eclogites' and their felsic host rocks across the eastern Himalaya from Everest to Bhutan, linking time to the pressure–temperature evolution precisely has proven difficult and the tectonic interpretations much debated (e.g. O'Brien, 2019; Wang et al., 2021). This difficulty has led to conflicting interpretations about what the ages mean with respect to eastern Himalayan tectonic evolution. The discovery and analysis of allanite and the recognition of the effect of melt infiltration in the NW Bhutan metabasite samples allow the metamorphic evolution of these metabasites to be more tightly constrained. Our data suggest that the metabasites now exposed in NW Bhutan experienced high-pressure conditions c. 19–17 Ma, recorded by the growth of garnet, rutile, Cpx1, Aln1 and Zrn1 in a plagioclase-free assemblage. Decompression then followed, with the growth of plagioclase- and orthopyroxene-present symplectitic assemblages replacing garnet and Cpx1, and these themselves then later being replaced by hornblende. Aln2 and Zrn2 record growth in a symplectite-forming and melt-present environment at c. 15–14 Ma. Previous studies in NW Bhutan have interpreted 15–11 Ma zircon and monazite in NW Bhutan migmatitic leucosomes and leucogranites as recording the timing of crystallization of decompression-related anatectic melts (Hopkinson et al., 2020; Kellett et al., 2009; Montomoli et al., 2013; Warren et al., 2011). Given the longevity of melt production and crystallization in the Himalaya (e.g. Lederer et al., 2013) and the lack of precise pressure–temperature–time points on the metamorphic path of these rocks, we do not feel our new data can constrain this part of the path any more tightly. Rutile in felsic granulites from NW Bhutan records cooling through their closure temperature at c. 11 Ma (Warren et al., 2012).

—WILEY 783

The peak metamorphic evolution of the NW Bhutan metabasites is somewhat shallower, cooler and younger than the metamorphic evolution and exhumation of similar rocks exposed further westwards in Sikkim, Ama Drime and in the Everest region (Corrie et al., 2010; Cottle et al., 2009; Kellett et al., 2014; Wang et al., 2021, 2017). No unambiguous evidence for relict omphacite has yet been reported in NW Bhutan, unlike in Dinggye, China (Wang et al., 2017), nor can plausible omphacite compositions be reconstructed from the symplectite compositions, unlike in Ama Drime (Groppo et al., 2007). These data suggest that the granulitized eclogites exposed in Tibet, Nepal and Sikkim either had protolith compositions that allowed omphacite to form or were metamorphosed at higher pressures than those exposed in NW Bhutan.

Peak temperatures for the Bhutan samples are poorly constrained due to the uncertainties in bulk composition and open system behaviour as noted above. However, it seems likely that peak temperatures were ∼650–750°C, that is, hot enough for partial melting to occur in the host metasediments and that the rocks remained hot during decompression to at least 1 GPa if not shallower depths. There is no apparent record of the ultra-high overprint temperatures of >900°C calculated for Everest East (Wang et al., 2021) in NW Bhutan.

Our new dates and interpretations provide evidence for the diachroneity of high-pressure metamorphism and exhumation across the central and eastern Himalaya. Monazite and zircon cores in felsic host rocks yielding dates of c. 30–29 Ma (Wang et al., 2021) and Lu–Hf dating of garnet in mafic rocks in Ama Drime at 37–34 Ma (Kellett et al., 2014) suggest high pressures prevailed there c. 10 Ma before high-pressure metamorphism in NW Bhutan. Similarly, 17–18 Ma metabasite zircon rims in Ama Drime (Li et al., 2003), and 21–19 Ma monazite and xenotime in the host metapelites (Wang et al., 2017) have been interpreted as recording the timing of decompression, with younger dates <15 Ma generally interpreted as recording the crystallization of decompression-related melts (Groppo et al., 2007; Kali et al., 2010; Wang et al., 2021, 2017). These dates are all somewhat older than corresponding points on the pressure–temperature–time path suggested here for NW Bhutan, though the timing of melt crystallization may be somewhat similar.

In Ama Drime, clear evidence for east–west extension has provided a tectonic mechanism for at least the later exhumation of the high-pressure rocks (reviewed in O'Brien et al 2019). In NW Bhutan there is no such evidence for late orogen-parallel extension associated with the high-pressure terrane. Instead, exhumation appears to have been accomplished by out-of-sequence thrusting perpendicular to the orogen, directed roughly southwards.

Previous studies have suggested a late-stage insertion of a 'tectonic plunger' (i.e. a ramp of cold rigid Indian lower-crust) into the lower-crust (Kellett et al., 2009; Warren et al., 2011). This mechanism provides the additional upwards driving force required to exhume lower orogenic crust that is neutrally buoyant compared to its surroundings (unlike, say, subduction-related eclogites; see O'Brien, 2019, for a succinct summary). Geophysical evidence for a ramp of colder, stronger Indian basement crust beneath Tibet (Nábělek et al., 2009) coupled with plate reconstructions that are suggestive of a slowing down of the India–Asia collision (Van Hinsbergen et al., 2012) over the timescale of interest provide further supporting evidence of this model.

6 | CONCLUSIONS

Petrographic observations and mineral data from metabasite samples in NW Bhutan, and especially sample EWB 071, suggest that evidence for the transition from a higher pressure plagioclase-absent garnet–clinopyroxene1–quartz–rutile assemblage to a lower pressure plagioclase-present (garnet)–clinopyroxene2–orthopyroxene–ilmenite assemblage was geochemically and geochronologically captured by the growth of two phases of allanite and zircon. Overall, the petrographic, elemental and isotope data suggest the following timing for the sequence of mineral growth:

i. Aln1 growth under high-pressure plagioclase-absent conditions at c. 19 Ma.
ii. Zrn1 growth under plagioclase-absent conditions at c. 17–15.5 Ma.
iii. Formation of Cpx2 + Pl ± Hbl symplectites during the decompression-related breakdown of Cpx1.
iv. Dissolution of Aln1, garnet, Zrn1 and rutile, and growth of REE-enriched Aln2 and Zrn2 between 15.5 and 14.0 Ma, likely in the presence of melt infiltrated from the host metasediments. Garnet dissolution was accompanied by the formation of Opx + Pl symplectites and a corona of Opx separating garnet and quartz.
v. Formation of symplectites of Ilm + Cpx around Aln2, suggestive of titanite breakdown.
vi. Replacement of Cpx2 and Opx by Hbl.

These samples record an excellent example of rare allanite growth and preservation in metabasites under high-temperature-low-pressure metamorphic conditions.

Despite the relative plethora of zircon and monazite isotopic and elemental data from metabasites that preserve similar metamorphic textures in the eastern

Himalaya, the precise linking of time to the pressure–temperature evolution has proven challenging for these samples from Bhutan. Our discovery of two chemically and texturally distinguishable allanite populations that are petrochronologically linkable both to the zircon record *and* to the textural evolution of the major rock-forming phases has enabled more unambiguous linkage of 'age to stage', despite the difficulty in constraining the precise P–T path.

Our new observations and data confirm previous suggestions of rapid exhumation of deep Himalayan crust during the Miocene at least in the eastern Himalaya. In comparison with data from similar rocks further westwards in the orogen, the new data suggest a younger and shallower history for NW Bhutan.

CONFLICT OF INTEREST STATEMENT

The authors declare no conflicts of interest.

ORCID

Clare J. Warren https://orcid.org/0000-0003-2444-9737
Barbara E. Kunz https://orcid.org/0000-0002-9492-1497
Tom W. Argles https://orcid.org/0000-0002-0484-4230
Alison Halton https://orcid.org/0000-0002-1931-5016

REFERENCES

Airaghi, L., Janots, E., Lanari, P., de Sigoyer, J., & Magnin, V. (2019). Allanite petrochronology in fresh and retrogressed garnet–biotite metapelites from the Longmen Shan (eastern Tibet). *Journal of Petrology*, 60(1), 151–176. https://doi.org/10.1093/petrology/egy109

Anderson, E. D., & Moecher, D. P. (2007). Omphacite breakdown reactions and relation to eclogite exhumation rates. *Contributions to Mineralogy and Petrology*, 154(3), 253–277. https://doi.org/10.1007/s00410-007-0192-x

Angiboust, S., & Harlov, D. (2017). Ilmenite breakdown and rutile–titanite stability in metagranitoids: Natural observations and experimental results. *American Mineralogist: Journal of Earth and Planetary Materials*, 102(8), 1696–1708. https://doi.org/10.2138/am-2017-6064

Baxter, E. F., Caddick, M. J., & Dragovic, B. (2017). Garnet: A rock-forming mineral petrochronometer. *Reviews in Mineralogy and Geochemistry*, 83(1), 469–533.

Carlson, W. D. (2012). Rates and mechanism of Y, REE, and Cr diffusion in garnet. *American Mineralogist*, 97(10), 1598–1618. https://doi.org/10.2138/am.2012.4108

Catlos, E. J., Sorensen, S. S., & Harrison, T. M. (2000). Th–Pb ion–microprobe dating of allanite. *American Mineralogist*, 85(5–6), 633–648. https://doi.org/10.2138/am-2000-5-601

Chakungal, J., Dostal, J., Grujic, D., Duchêne, S., & Ghalley, K. S. (2010). Provenance of the greater Himalayan sequence: Evidence from mafic granulites and amphibolites in NW Bhutan. *Tectonophysics*, 480(1), 198–212. https://doi.org/10.1016/j.tecto.2009.10.014

Corrie, S. L., Kohn, M. J., & Vervoort, J. D. (2010). Young eclogite from the greater Himalayan sequence, Arun Valley, eastern Nepal: P–T–t path and tectonic implications. *Earth and Planetary Science Letters*, 289(3), 406–416. https://doi.org/10.1016/j.epsl.2009.11.029

Cottle, J. M., Jessup, M. J., Newell, D. L., Horstwood, M. S. A., Noble, S. R., Parrish, R. R., Waters, D. J., & Searle, M. P. (2009). Geochronology of granulitized eclogite from the Ama Drime massif: Implications for the tectonic evolution of the south Tibetan Himalaya. *Tectonics*, 28(1). https://doi.org/10.1029/2008TC002256

Crisp, L. J., Berry, A. J., Burnham, A. D., Miller, L. A., & Newville, M. (2023). The Ti-in-zircon thermometer revised: The effect of pressure on the Ti site in zircon. *Geochimica et Cosmochimica Acta*, 360, 241–258. https://doi.org/10.1016/j.gca.2023.04.031

Darling, J. R., Storey, C. D., & Engi, M. (2012). Allanite U–Th–Pb geochronology by laser ablation ICPMS. *Chemical Geology*, 292, 103–115. https://doi.org/10.1016/j.chemgeo.2011.11.012

de Capitani, C., & Petrakakis, K. (2010). The computation of equilibrium assemblage diagrams with Theriak/domino software. *American Mineralogist*, 95(7), 1006–1016. https://doi.org/10.2138/am.2010.3354

Degeling, H., Eggins, S., & Ellis, D. J. (2001). Zr budgets for metamorphic reactions, and the formation of zircon from garnet breakdown. *Mineralogical Magazine*, 65(6), 749–758. https://doi.org/10.1180/0026461016560006

El Korh, A. (2014). Ablation behaviour of allanites during U–Th–Pb dating using a quadrupole ICP-MS coupled to a 193 nm excimer laser. *Chemical Geology*, 371, 46–59. https://doi.org/10.1016/j.chemgeo.2014.01.021

Engi, M. (2017). Petrochronology based on REE-minerals: Monazite, allanite, xenotime, apatite. *Reviews in Mineralogy and Geochemistry*, 83(1), 365–418. https://doi.org/10.2138/rmg.2017.83.12

Faryad, S. W., Nahodilová, R., & Dolejš, D. (2010). Incipient eclogite facies metamorphism in the Moldanubian granulites revealed by mineral inclusions in garnet. *Lithos*, 114(1–2), 54–69. https://doi.org/10.1016/j.lithos.2009.07.014

Faryad, S. W., Perraki, M., & Vrána, S. (2006). P–T evolution and reaction textures in retrogressed eclogites from Svetlik, the Moldanubian zone (Czech Republic). *Mineralogy and Petrology*, 88(1), 297–319. https://doi.org/10.1007/s00710-006-0142-8

Ferry, J. M., & Watson, E. B. (2007). New thermodynamic models and revised calibrations for the Ti-in-zircon and Zr-in-rutile thermometers. *Contributions to Mineralogy and Petrology*, *154*(4), 429–437. https://doi.org/10.1007/s00410-007-0201-0

Franz, G., Thomas, S., & Smith, D. C. (1986). High-pressure phengite decomposition in the Weissenstein eclogite, Münchberger Gneiss Massif, Germany. *Contributions to Mineralogy and Petrology*, *92*(1), 71–85. https://doi.org/10.1007/BF00373964

Frost, B. R., Chamberlain, K. R., & Schumacher, J. C. (2001). Sphene (titanite): Phase relations and role as a geochronometer. *Chemical Geology*, *172*(1–2), 131–148. https://doi.org/10.1016/S0009-2541(00)00240-0

Gieré, R., & Sorensen, S. S. (2004). Allanite and other REE-rich epidote-group minerals. *Reviews in Mineralogy and Geochemistry*, *56*(1), 431–493. https://doi.org/10.2138/gsrmg.56.1.431

Goswami-Banerjee, S., & Robyr, M. (2015). Pressure and temperature conditions for crystallization of metamorphic allanite and monazite in metapelites: A case study from the Miyar Valley (high Himalayan crystalline of Zanskar, NW India). *Journal of Metamorphic Geology*, *33*(5), 535–556. https://doi.org/10.1111/jmg.12133

Gregory, C. J., Buick, I. S., Hermann, J., & Rubatto, D. (2009). Mineral-scale trace element and U–Th–Pb age constraints on metamorphism and melting during the Petermann orogeny (Central Australia). *Journal of Petrology*, *50*(2), 251–287. https://doi.org/10.1093/petrology/egn077

Gregory, C. J., Rubatto, D., Allen, C. M., Williams, I. S., Hermann, J., & Ireland, T. (2007). Allanite micro-geochronology: A LA-ICP-MS and SHRIMP U–Th–Pb study. *Chemical Geology*, *245*(3–4), 162–182. https://doi.org/10.1016/j.chemgeo.2007.07.029

Gregory, C. J., Rubatto, D., Hermann, J., Berger, A., & Engi, M. (2012). Allanite behaviour during incipient melting in the southern Central Alps. *Geochimica et Cosmochimica Acta*, *84*, 433–458. https://doi.org/10.1016/j.gca.2012.01.020

Groppo, C., Lombardo, B., Rolfo, F., & Pertusati, P. (2007). Clockwise exhumation path of granulitized eclogites from the Ama Drime range (eastern Himalayas). *Journal of Metamorphic Geology*, *25*(1), 51–75. https://doi.org/10.1111/j.1525-1314.2006.00678.x

Grujic, D., Warren, C. J., & Wooden, J. L. (2011). Rapid synconvergent exhumation of Miocene-aged lower orogenic crust in the eastern Himalaya. *Lithosphere*, *3*(5), 346–366. https://doi.org/10.1130/L154.1

Hermann, J. (2002). Allanite: Thorium and light rare earth element carrier in subducted crust. *Chemical Geology*, *192*(3–4), 289–306. https://doi.org/10.1016/S0009-2541(02)00222-X

Hinton, R. W., & Upton, B. G. J. (1991). The chemistry of zircon: Variations within and between large crystals from syenite and alkali basalt xenoliths. *Geochimica et Cosmochimica Acta*, *55*(11), 3287–3302. https://doi.org/10.1016/0016-7037(91)90489-R

Holland, T. J. B., & Powell, R. T. J. B. (1998). An internally consistent thermodynamic data set for phases of petrological interest. *Journal of Metamorphic Geology*, *16*(3), 309–343. https://doi.org/10.1111/j.1525-1314.1998.00140.x

Hopkinson, T., Harris, N., Roberts, N. M. W., Warren, C. J., Hammond, S., Spencer, C. J., & Parrish, R. R. (2020). Evolution of the melt source during protracted crustal anatexis: An example from the Bhutan Himalaya. *Geology*, *48*(1), 87–91. https://doi.org/10.1130/G47078.1

Horstwood, M. S. A., Košler, J., Gehrels, G., Jackson, S. E., McLean, N. M., Paton, C., Pearson, N. J., Sircombe, K., Sylvester, P., & Vermeesch, P. (2016). Community-derived standards for LA-ICP-MSU-(Th-)Pb geochronology—Uncertainty propagation, age interpretation and data reporting. *Geostandards and Geoanalytical Research*, *40*(3), 311–332. https://doi.org/10.1111/j.1751-908X.2016.00379.x

Janots, E., Brunet, F., Goffé, B., Poinssot, C., Burchard, M., & Cemič, L. (2007). Thermochemistry of monazite-(La) and dissakisite-(La): Implications for monazite and allanite stability in metapelites. *Contributions to Mineralogy and Petrology*, *154*(1), 1–14. https://doi.org/10.1007/s00410-006-0176-2

Janots, E., Engi, M., Berger, A., Allaz, J., Schwarz, J., & Spandler, C. (2008). Prograde metamorphic sequence of REE minerals in pelitic rocks of the Central Alps: Implications for allanite–monazite–xenotime phase relations from 250 to 610 C. *Journal of Metamorphic Geology*, *26*(5), 509–526. https://doi.org/10.1111/j.1525-1314.2008.00774.x

Janots, E., Engi, M., Rubatto, D., Berger, A., Gregory, C., & Rahn, M. (2009). Metamorphic rates in collisional orogeny from in situ allanite and monazite dating. *Geology*, *37*(1), 11–14. https://doi.org/10.1130/G25192A.1

Kali, E., Leloup, P. H., Arnaud, N., Mahéo, G., Liu, D., Boutonnet, E., Van der Woerd, J., Liu, X., Liu-Zeng, J., & Li, H. (2010). Exhumation history of the deepest central Himalayan rocks, Ama Drime range: Key pressure–temperature–deformation–time constraints on orogenic models. *Tectonics*, *29*(2), n/a. https://doi.org/10.1029/2009TC002551

Kellett, D. A., Cottle, J. M., & Smit, M. (2014). Eocene deep crust at Ama Drime, Tibet: Early evolution of the Himalayan orogen. *Lithosphere*, *6*(4), 220–229. https://doi.org/10.1130/L350.1

Kellett, D., Grujic, D., & Erdmann, S. (2009). Miocene structural reorganization of the south Tibetan detachment, eastern Himalaya: Implications for continental collision. *Lithosphere*, *1*(5), 259–281. https://doi.org/10.1130/L56.1

Kohn, M. J., Engi, M., & Lanari, P. (2017). Petrochronology. *Methods and Applications, Mineralogical Society of America Reviews in Mineralogy and Geochemistry*, *83*, 575.

Kunz, B. E., Regis, D., & Engi, M. (2018). Zircon ages in granulite facies rocks: Decoupling from geochemistry above 850°C? *Contributions to Mineralogy and Petrology*, *173*, 26. https://doi.org/10.1007/s00410-018-1454-5

Kusiak, M. A., Whitehouse, M. J., Wilde, S. A., Nemchin, A. A., & Clark, C. (2013). (2013) mobilization of radiogenic Pb in zircon revealed by ion imaging: Implications for early earth geochronology. *Geology*, *4*(3), 291–294. https://doi.org/10.1130/G33920.1

Lanari, P., & Engi, M. (2017). Local bulk composition effects on metamorphic mineral assemblages. *Reviews in Mineralogy and Geochemistry*, *83*(1), 55–102. https://doi.org/10.2138/rmg.2017.83.3

Lanari, P., Vidal, O., De Andrade, V., Dubacq, B., Lewin, E., Grosch, E. G., & Schwartz, S. (2014). XMa P-tools: A MATLAB©-based program for electron microprobe X-ray image processing and geothermobarometry. *Computers & Geosciences*, *62*, 227–240. https://doi.org/10.1016/j.cageo.2013.08.010

Leake, B. E. (1978). Nomenclature of amphiboles. *American Mineralogist*, *63*(11–12), 1023–1052.

Lederer, G. L., Cottle, J., Jessup, M., Langille, J., & Ahmad, T. (2013). Timescales of partial melting in the Himalayan middle crust: Insight from the Leo Pargil dome, Northwest India. *Contributions to Mineralogy and Petrology*, *166*, 1415–1441. https://doi.org/10.1007/s00410-013-0935-9

Li, D., Liao, Q., Yuan, Y., Wan, Y., Liu, D., Zhang, X., Yi, S., Cao, S., & Xie, D. (2003). SHRIMP U-Pb zircon geochronology of granulites at Rimana (southern Tibet) in the central segment of Himalayan Orogen. *Chinese Science Bulletin*, *48*(23), 2647–2650. https://doi.org/10.1360/03wd0080

Liu, Y., Siebel, W., Massonne, H.-J., & Xiao, X. (2007). Geochronological and petrological constraints for tectonic evolution of the central greater Himalayan sequence in the Kharta area, southern Tibet. *The Journal of Geology*, *115*(2), 215–230. https://doi.org/10.1086/510806

Lombardo, B., & Rolfo, F. (2000). Two contrasting eclogite types in the Himalayas: Implications for the Himalayan orogeny. *Journal of Geodynamics*, *30*(1), 37–60. https://doi.org/10.1016/S0264-3707(99)00026-5

Lombardo, B., Rolfo, F., & McClelland, W. C. (2016). A review of the first eclogites discovered in the eastern Himalaya. *European Journal of Mineralogy*, *28*(6), 1099–1109. https://doi.org/10.1127/ejm/2016/0028-2553

Loury, C., Rolland, Y., Cenki-Tok, B., Lanari, P., & Guillot, S. (2016). Late Paleozoic evolution of the south Tien Shan: Insights from P–T estimates and allanite geochronology on retrogressed eclogites (Chatkal range, Kyrgyzstan). *Journal of Geodynamics*, *96*, 62–80. https://doi.org/10.1016/j.jog.2015.06.005

Marsh, J. H., & Kelly, E. D. (2017). Petrogenetic relations among titanium-rich minerals in an anatectic high-P mafic granulite. *Journal of Metamorphic Geology*, *35*(7), 717–738. https://doi.org/10.1111/jmg.12252

Marsh, J. H., & Smye, A. J. (2017). U-Pb systematics and trace element characteristics in titanite from a high-pressure mafic granulite. *Chemical Geology*, *466*, 403–416. https://doi.org/10.1016/j.chemgeo.2017.06.029

Matthews, A., & Goldsmith, J. R. (1984). The influence of metastability on reaction kinetics involving zoisite formation from anorthite at elevated pressures and temperatures. *American Mineralogist*, *69*(9–10), 848–857.

McFarlane, C. R. M. (2016). Allanite UPb geochronology by 193 nm LA ICP-MS using NIST610 glass for external calibration. *Chemical Geology*, *438*, 91–102. https://doi.org/10.1016/j.chemgeo.2016.05.026

Möller, C. (1998). Decompressed eclogites in the Sveconorwegian (−Grenvillian) orogen of SW Sweden: Petrology and tectonic implications. *Journal of Metamorphic Geology*, *16*(5), 641–656. https://doi.org/10.1111/j.1525-1314.1998.00160.x

Möller, C., Andersson, J., Dyck, B., & Lundin, I. A. (2015). Exhumation of an eclogite terrane as a hot migmatitic nappe, Sveconorwegian orogen. *Lithos*, *226*, 147–168. https://doi.org/10.1016/j.lithos.2014.12.013

Montomoli, C., Iaccarino, S., Carosi, R., Langone, A., & Visonà, D. (2013). Tectonometamorphic discontinuities within the greater Himalayan sequence in Western Nepal (central Himalaya):

Insights on the exhumation of crystalline rocks. *Tectonophysics*, *608*, 1349–1370. https://doi.org/10.1016/j.tecto.2013.06.006

Mottram, C. M., Warren, C. J., Regis, D., Roberts, N. M., Harris, N. B., Argles, T. W., & Parrish, R. R. (2014). Developing an inverted Barrovian sequence; insights from monazite petrochronology. *Earth and Planetary Science Letters*, *403*, 418–431. https://doi.org/10.1016/j.epsl.2014.07.006

Murali, A. V., Parthasarathy, R., Mahadevan, T. M., & Das, M. S. (1983). Trace element characteristics, REE patterns and partition coefficients of zircons from different geological environments—A case study on Indian zircons. *Geochimica et Cosmochimica Acta*, *47*(11), 2047–2052. https://doi.org/10.1016/0016-7037(83)90220-X

Nábělek, J., Hetényi, G., Vergne, J., Sapkota, S., Kafle, B., Jiang, M., Su, H., Chen, J., Huang, B.-S., & the Hi-CLIMB team. (2009). Underplating in the Himalaya-Tibet collision zone revealed by the hi-CLIMB experiment. *Science*, *325*(5946), 1371–1374. https://doi.org/10.1126/science.1167719

Oberli, F., Meier, M., Berger, A., Rosenberg, C. L., & GierÉ, R. (2004). U-Th-Pb and 230Th/238U disequilibrium isotope systematics: Precise accessory mineral chronology and melt evolution tracing in the Alpine Bergell intrusion. *Geochimica et Cosmochimica Acta*, *68*(11), 2543–2560. https://doi.org/10.1016/j.gca.2003.10.017

O'Brien, P. J. (2019). Eclogites and other high-pressure rocks in the Himalaya: A review. *Geological Society, London, Special Publications*, *483*(1), 183–213. https://doi.org/10.1144/SP483.13

O'Brien, P. J., & Rötzler, J. (2003). High-pressure granulites: Formation, recovery of peak conditions and implications for tectonics. *Journal of Metamorphic Geology*, *21*(1), 3–20. https://doi.org/10.1046/j.1525-1314.2003.00420.x

Otamendi, J. E., de La Rosa, J. D., Douce, A. E. P., & Castro, A. (2002). Rayleigh fractionation of heavy rare earths and yttrium during metamorphic garnet growth. *Geology*, *30*(2), 159–162. https://doi.org/10.1130/0091-7613(2002)030<0159:RFOHRE>2.0.CO;2

Pereira, I., & Storey, C. D. (2023). Detrital rutile: Records of the deep crust, ores and fluids. *Lithos*, *438-439*, 107010. https://doi.org/10.1016/j.lithos.2022.107010

Regis, D., Warren, C. J., Mottram, C. M., & Roberts, N. M. (2016). Using monazite and zircon petrochronology to constrain the *P–T–t* evolution of the middle crust in the Bhutan Himalaya. *Journal of Metamorphic Geology*, *34*(6), 617–639. https://doi.org/10.1111/jmg.12196

Regis, D., Warren, C. J., Young, D., & Roberts, N. M. W. (2014). Tectono-metamorphic evolution of the Jomolhari massif: Variations in timing of syn-collisional metamorphism across western Bhutan. *Lithos*, *190–191*, 449–466. https://doi.org/10.1016/j.lithos.2014.01.001

Robyr, M., Carosi, R., Iaccarino, S., & Montmoli, C. (2023). The greater Himalayan sequence-tectonic, petrographic and kinematic evolution of the metamorphic Core zone of the Himalayan. *Himalaya: Dynamics of a Giant, Tectonic Units and Structure of the Himalaya*, *2*, 105.

Rolfo, F., Carosi, R., Montomoli, C., & Visonà, D. (2008). Discovery of granulitized eclogite in North Sikkim expands the eastern Himalaya high-pressure province. *Himalayan Journal of Sciences*, *5*(7), 126–127. https://doi.org/10.3126/hjs.v5i7.1312

Rubatto, D. (2002). Zircon trace element geochemistry: Partitioning with garnet and the link between U–Pb ages and metamorphism. *Chemical Geology*, *184*(1), 123–138. https://doi.org/10.1016/S0009-2541(01)00355-2

Rubatto, D. (2017). Zircon: The metamorphic mineral. *Reviews in Mineralogy and Geochemistry*, *83*(1), 261–295. https://doi.org/10.2138/rmg.2017.83.9

Rubatto, D., Burger, M., Lanari, P., Hattendorf, B., Schwarz, G., Neff, C., Keresztes Schmidt, P., Hermann, J., Vho, A., & Günther, D. (2020). Identification of growth mechanisms in metamorphic garnet by high-resolution trace element mapping with LA-ICP-TOFMS. *Contributions to Mineralogy and Petrology*, *175*(7), 61. https://doi.org/10.1007/s00410-020-01700-5

Rubatto, D., Chakraborty, S., & Dasgupta, S. (2013). Timescales of crustal melting in the higher Himalayan crystallines (Sikkim, eastern Himalaya) inferred from trace element-constrained monazite and zircon chronology. *Contributions to Mineralogy and Petrology*, *165*, 349–372. https://doi.org/10.1007/s00410-012-0812-y

Rubatto, D., Regis, D., Hermann, J., Boston, K., Engi, M., Beltrando, M., & McAlpine, S. R. (2011). Yo-yo subduction recorded by accessory minerals in the Italian Western Alps. *Nature Geoscience*, *4*(5), 338–342.

Skora, S., Baumgartner, L. P., Mahlen, N. J., Johnson, C. M., Pilet, S., & Hellebrand, E. (2006). Diffusion-limited REE uptake by eclogite garnets and its consequences for Lu–Hf and Sm–Nd geochronology. *Contributions to Mineralogy and Petrology*, *152*(6), 703–720. https://doi.org/10.1007/s00410-006-0128-x

Smye, A. J., Bickle, M. J., Holland, T. J. B., Parrish, R. R., & Condon, D. J. (2011). Rapid formation and exhumation of the youngest Alpine eclogites: A thermal conundrum to Barrovian metamorphism. *Earth and Planetary Science Letters*, *306*(3–4), 193–204. https://doi.org/10.1016/j.epsl.2011.03.037

Smye, A. J., Roberts, N. M. W., Condon, D. J., Horstwood, M. S. A., & Parrish, R. R. (2014). Characterising the U–Th–Pb systematics of allanite by ID and LA-ICPMS: Implications for geochronology. *Geochimica et Cosmochimica Acta*, *135*, 1–28. https://doi.org/10.1016/j.gca.2014.03.021

Sorensen, S. S. (1991). Petrogenetic significance of zoned allanite in garnet amphibolites from a paleo-subduction zone: Catalina schist, southern California. *American Mineralogist*, *76*(3–4), 589–601.

Spear, F. S. (2010). Monazite–allanite phase relations in metapelites. *Chemical Geology*, *279*(1–2), 55–62. https://doi.org/10.1016/j.chemgeo.2010.10.004

Spencer, C. J., Roberts, N. M. W., Cawood, P. A., Hawkesworth, C. J., Prave, A. R., Antonini, A. S. M., & Horstwood, M. S. A. (2014). Intermontane basins and bimodal volcanism at the onset of the Sveconorwegian orogeny, southern Norway. *Precambrian Research*, *252*, 107–118. https://doi.org/10.1016/j.precamres.2014.07.008

Stacey, J. S., & Kramers, J. D. (1975). Approximation of terrestrial lead isotope evolution by a two-stage model. *Earth and Planetary Science Letters*, *26*(2), 207–221. https://doi.org/10.1016/0012-821X(75)90088-6

St-Onge, M. R., Rayner, N., Palin, R. M., Searle, M. P., & Waters, D. J. (2013). Integrated pressure–temperature–time constraints for the Tso Morari dome (Northwest India): Implications for the burial and exhumation path of UHP units in the western Himalaya. *Journal of Metamorphic Geology*, *31*(5), 469–504. https://doi.org/10.1111/jmg.12030

Thakur, S. S., Madhavan, K., Patel, S. C., Rao, D. R., Singh, A. K., Pandey, S., & Nandini, P. (2018). Yttrium-zoning in garnet and stability of allanite in metapelites from the Main Central Thrust Zone and adjacent higher Himalayan crystallines along the Alaknanda Valley, NW Himalaya. *Lithos*, *320*, 1–19. https://doi.org/10.1016/j.lithos.2018.09.002

Van Hinsbergen, D. J., Lippert, P. C., Dupont-Nivet, G., McQuarrie, N., Doubrovine, P. V., Spakman, W., & Torsvik, T. H. (2012). Greater India Basin hypothesis and a two-stage Cenozoic collision between India and Asia. *Proceedings of the National Academy of Sciences*, *109*(20), 7659–7664. https://doi.org/10.1073/pnas.1117262109

Vermeesch, P. (2018). IsoplotR: A free and open toolbox for geochronology. *Geoscience Frontiers*, *9*(5), 1479–1493. https://doi.org/10.1016/j.gsf.2018.04.001

Vermeesch, P. (2020). Unifying the U–Pb and Th–Pb methods: Joint isochron regression and common Pb correction. *Geochronology*, *2*(1), 119–131.

Wang, J.-M., Lanari, P., Wu, F.-Y., Zhang, J.-J., Khanal, G. P., & Yang, L. (2021). First evidence of eclogites overprinted by ultrahigh temperature metamorphism in Everest east, Himalaya: Implications for collisional tectonics on early earth. *Earth and Planetary Science Letters*, *558*, 116760. https://doi.org/10.1016/j.epsl.2021.116760

Wang, Y., Zhang, L., Zhang, J., & Wei, C. (2017). The youngest eclogite in central Himalaya: P–T path, U–Pb zircon age and its tectonic implication. *Gondwana Research*, *41*, 188–206. https://doi.org/10.1016/j.gr.2015.10.013

Warren, C. J., Grujic, D., Cottle, J. M., & Rogers, N. W. (2012). Constraining cooling histories: Rutile and titanite chronology and diffusion modelling in NW Bhutan. *Journal of Metamorphic Geology*, *30*, 113–130. https://doi.org/10.1111/j.1525-1314.2011.00958.x

Warren, C. J., Grujic, D., Kellett, D. A., Cottle, J., Jamieson, R. A., & Ghalley, K. S. (2011). Probing the depths of the India–Asia collision: U–Th–Pb monazite chronology of granulites from NW Bhutan. *Tectonics*, *30*(2). https://doi.org/10.1029/2010TC002738

Weller, O. M., St-Onge, M. R., Waters, D. J., Rayner, N., Searle, M. P., Chung, S. L., Palin, R. M., Lee, Y. H., & Xu, X. (2013). Quantifying Barrovian metamorphism in the Danba structural culmination of eastern Tibet. *Journal of Metamorphic Geology*, *31*(9), 909–935. https://doi.org/10.1111/jmg.12050

Whitney, D. L., & Evans, B. W. (2010). Abbreviations for names of rock-forming minerals. *American Mineralogist*, *95*(1), 185–187. https://doi.org/10.2138/am.2010.3371

Zhao, G., Cawood, P. A., Wilde, S. A., & Lu, L. (2001). High-pressure granulites (retrograded eclogites) from the Hengshan complex, North China craton: Petrology and tectonic implications. *Journal of Petrology*, *42*(6), 1141–1170. https://doi.org/10.1093/petrology/42.6.1141

SUPPORTING INFORMATION

Additional supporting information can be found online in the Supporting Information section at the end of this article.

Data S1. Supporting Information.
Data S2. Supporting Information.
Data S3. Supporting Information.
Data S4. Supporting Information.
Data S5. Supporting Information.
Data S6. Supporting Information.